Microscopic study of low-lying spectra of Λ hypernuclei based on a beyond-mean-field approach with a covariant energy density functional

H. Mei,[1,2] K. Hagino,[1,3] J. M. Yao,[1,2] and T. Motoba[4,5]
[1]*Department of Physics, Tohoku University, Sendai 980-8578, Japan*
[2]*School of Physical Science and Technology, Southwest University, Chongqing 400715, China*
[3]*Research Center for Electron Photon Science, Tohoku University, 1-2-1 Mikamine, Sendai 982-0826, Japan*
[4]*Laboratory of Physics, Osaka Electro-communication University, Neyagawa 572-8530, Japan*
[5]*Yukawa Institute for Theoretical Physics, Kyoto University, Kyoto 606-8502, Japan*
(Received 19 April 2015; published 8 June 2015)

We present a detailed formalism of the microscopic particle-rotor model for hypernuclear low-lying states based on a covariant density functional theory. In this method, the hypernuclear states are constructed by coupling a hyperon to low-lying states of the core nucleus, which are described by the generator coordinate method (GCM) with the particle number and angular momentum projections. We apply this method to study in detail the low-lying spectrum of ${}^{13}_{\Lambda}$C and ${}^{21}_{\Lambda}$Ne hypernuclei. We also briefly discuss the structure of ${}^{155}_{\Lambda}$Sm as an example of heavy deformed hypernuclei. It is shown that the low-lying excitation spectra with positive-parity states of the hypernuclei, which are dominated by Λ hyperon in the *s* orbital coupled to the core states, are similar to that for the corresponding core states, while the electric quadrupole transition strength, $B(E2)$, from the 2^+_1 state to the ground state is reduced according to the mass number of the hypernuclei. Our study indicates that the energy splitting between the first $1/2^-$ and $3/2^-$ hypernuclear states is generally small for all the hypernuclei which we study. However, their configurations depend much on the properties of a core nucleus, in particular on the sign of deformation parameter. That is, the first $1/2^-$ and $3/2^-$ states in ${}^{13}_{\Lambda}$C are dominated by a single configuration with Λ particle in the *p*-wave orbits and thus provide good candidates for a study of the Λ spin-orbit splitting. On the other hand, those states in the other hypernuclei exhibit a large configuration mixing and thus their energy difference cannot be interpreted as the spin-orbit splitting for the *p* orbits.

DOI: 10.1103/PhysRevC.91.064305 PACS number(s): 21.80.+a, 23.20.−g, 21.60.Jz, 21.10.−k

I. INTRODUCTION

The development in Λ-hypernuclear spectroscopy has enabled one to explore several aspects of hypernuclear structure [1,2]. Since hyperon-nucleon and hyperon-hyperon scattering experiments are difficult to perform, the information on the ΛN and ΛΛ interactions have been extracted from such studies. Moreover, since a Λ hyperon is free from the Pauli principle from other nucleons, it can go deeply inside a nucleus, which can also be used as a sensitive probe in order to study the structure of normal nuclei. Theoretically, many methods have been developed to investigate the spectroscopy of hypernuclei, such as the cluster model [3–9], the shell model [10–12], the *ab initio* method [13], the antisymmetrized molecular dynamics (AMD) [14–17], and self-consistent mean-field models [18–26]. Among them, the self-consistent mean-field approach is the only microscopic method which can be globally applied from light to heavy hypernuclei.

One of the characteristic features of atomic nuclei is deformation in the body-fixed frame. In the mean-field approach, the optimized deformation is automatically obtained by minimizing the total energy of a system in the mean-field approximation. It was shown, however, that the potential energy surface of a hypernucleus is generally softer against deformation than that of the corresponding core nucleus [21]. This implies that the shape fluctuation effect, which is not included in the pure mean-field approximation, will be more important in hypernuclei than in normal nuclei. Furthermore, in order to connect mean-field results to spectroscopic observables, such as $B(E2)$ values, one has to transform the results to the laboratory frame. To this end, one has to rely on additional assumptions such as the rigid rotor model, which, however, would not work for, e.g., nuclei with small deformation or with shape coexistence. To quantify the impurity effect of Λ particle on nuclear structure, one thus has to go beyond the pure mean-field approximation.

In our previous publication [27], we have proposed a new approach using a microscopic particle-rotor model (PRM) for the low-lying states of single-Λ hypernuclei. In this method, the Λ particle is coupled to the core nucleus states while the Λ hyperon interacts with the nucleons inside the nuclear core. For the core nucleus, a beyond-relativistic-mean-field approach is applied for low-lying states by carrying out the angular momentum and the particle number projections as well as the configuration mixing with the generator coordinate method (GCM). We have successfully applied this method to the spectrum of ${}^{9}_{\Lambda}$Be.

The motivation of the present work is to introduce a detailed formalism of this method. At the same time, we also apply it systematically in order to study the low-lying states of single-Λ hypernuclei in the mass region from light to heavy. For this purpose, we first discuss the ${}^{13}_{\Lambda}$C hypernucleus, which is an ideal hypernucleus in order to discuss the spin-orbit splitting. We then discuss ${}^{21}_{\Lambda}$Ne as an example of hypernuclei in the *sd*-shell region with a prolate deformation. The ${}^{155}_{\Lambda}$Sm hypernucleus, which is a well-deformed system and has a well-developed ground-state rotational band, is also considered as an example of heavy hypernuclei.

The paper is organized as follows. In Sec. II we present a detailed introduction to the formalism of microscopic PRM based on the covariant density functional theory (CDFT). In Sec. III, the results for the low-lying states of hypernuclei and the corresponding core nuclei are presented. Finally, we summarize the conclusions of this paper in Sec. IV.

II. MICROSCOPIC PARTICLE-ROTOR MODEL FOR Λ HYPERNUCLEI

A. Coupled-channels equations

The basic idea of the microscopic PRM for a single-Λ hypernucleus is that the valence Λ hyperon couples to the low-lying states of nuclear core, as is illustrated in a schematic picture of Fig. 1. In this approach, a hypernucleus is described in the laboratory frame and the wave function of the whole Λ hypernucleus is constructed as

$$\Psi_{JM}(\boldsymbol{r},\{\boldsymbol{r}_N\}) = \sum_{n,j,\ell,I} \mathscr{R}_{j\ell I_n}(r)\mathscr{F}^{JM}_{j\ell I_n}(\hat{\boldsymbol{r}},\{\boldsymbol{r}_N\}), \tag{1}$$

where

$$\mathscr{F}^{JM}_{j\ell I_n}(\hat{\boldsymbol{r}},\{\boldsymbol{r}_N\}) = [\mathscr{Y}_{j\ell}(\hat{\boldsymbol{r}}) \otimes \Phi_{I_n}(\{\boldsymbol{r}_N\})]^{(JM)} \tag{2}$$

with $\boldsymbol{r}$ and $\boldsymbol{r}_N$ being the coordinates of the Λ hyperon and the nucleons, respectively. J is the angular momentum for the whole system while M is its projection onto the z axis. $\mathscr{Y}_{j\ell}(\hat{\boldsymbol{r}})$ is the spin-angular wave function for the Λ hyperon. $|\Phi_{I_n}\rangle$ is the wave functions of the low-lying states of nuclear core, where I represents the angular momentum of the core state and $n = 1,2,\ldots$ distinguish different core states with the same angular momentum I. For convenience, hereafter we introduce the shorthand notation $k = \{j\ell I_n\}$ to represent different channels.

In the relativistic approach, $\mathscr{R}_k(r)$ is the radial wave function of a four-component Dirac spinor and it can be written

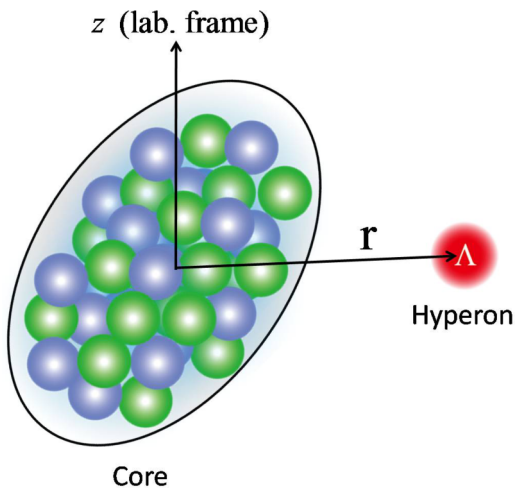

FIG. 1. (Color online) A schematic picture of the microscopic particle-rotor model for Λ hypernucleus, in which $\boldsymbol{r}$ denotes the coordinate of the Λ hyperon. In this approach, the nuclear core states are described microscopically with the multireference density functional theory.

in the following form:

$$\mathscr{R}_k(r) = \begin{pmatrix} f_k(r) \\ ig_k(r)\boldsymbol{\sigma}\cdot\hat{\boldsymbol{r}} \end{pmatrix}. \tag{3}$$

The Hamiltonian $\hat{H}$ for the whole Λ hypernucleus can be written as

$$\hat{H} = \hat{T}_\Lambda + \sum_{i=1}^{A_c}\left[\hat{V}_V^{(N\Lambda)}(\boldsymbol{r},\boldsymbol{r}_{N_i}) + \hat{V}_S^{(N\Lambda)}(\boldsymbol{r},\boldsymbol{r}_{N_i})\right] + \hat{H}_c, \tag{4}$$

where A_c is the mass number of the core nucleus. The first term in Eq. (4), $\hat{T}_\Lambda$, is the kinetic energy of Λ hyperon,

$$\hat{T}_\Lambda = -i\boldsymbol{\alpha}\cdot\nabla_\Lambda + \gamma^0 m_\Lambda. \tag{5}$$

Here, m_Λ is the mass of the Λ hyperon and α and γ^0 are Dirac matrices. The second term in Eq. (4) represents the $N\Lambda$ interaction term between the valence Λ and the nucleons in the core nucleus. It is composed of both a repulsive vector-type term $\hat{V}_V^{(N\Lambda)}$ and an attractive scalar-type term $\hat{V}_S^{(N\Lambda)}$, for which we take the following contact coupling forms:

$$\hat{V}_V^{(N\Lambda)}(\boldsymbol{r},\boldsymbol{r}_N) = \alpha_V^{N\Lambda}\delta(\boldsymbol{r}-\boldsymbol{r}_N), \tag{6}$$

$$\hat{V}_S^{(N\Lambda)}(\boldsymbol{r},\boldsymbol{r}_N) = \alpha_S^{N\Lambda}\gamma_\Lambda^0\delta(\boldsymbol{r}-\boldsymbol{r}_N)\gamma_N^0. \tag{7}$$

These $N\Lambda$ interactions correspond to the leading-order four-fermion coupling terms in the effective interaction proposed in Ref. [28]. For simplicity, the possible higher-order derivative and tensor coupling terms are neglected in the present study. We note here that the spin-orbit interaction of hyperon is automatically taken into account in the relativistic framework without introducing an additional parameter. The last term in Eq. (4) is the many-body Hamiltonian for the core nucleus satisfying the equation $\hat{H}_c|\Phi_{I_n}\rangle = E_{I_n}|\Phi_{I_n}\rangle$. In this paper, we use H_c that corresponds to the following point-coupling energy density functional (EDF) [29],

$$\begin{aligned} E_c[\{\rho_i\},\{j_i^\mu\}] &= \mathrm{Tr}[(\alpha\cdot\mathbf{p}+\beta m)\rho_V] \\ &+ \int d\boldsymbol{r}\Big(\frac{\alpha_S}{2}\rho_S^2 + \frac{\beta_S}{3}\rho_S^3 + \frac{\gamma_S}{4}\rho_S^4 \\ &+ \frac{\delta_S}{2}\rho_S\triangle\rho_S + \frac{\alpha_V}{2}j_\mu j^\mu + \frac{\gamma_V}{4}(j_\mu j^\mu)^2 \\ &+ \frac{\delta_V}{2}j_\mu\triangle j^\mu + \frac{\alpha_{TV}}{2}j_{TV}^\mu(j_{TV})_\mu \\ &+ \frac{\delta_{TV}}{2}j_{TV}^\mu\triangle(j_{TV})_\mu + \frac{e}{2}j_p^\mu A_\mu\Big), \end{aligned} \tag{8}$$

where A^μ is the four-component electromagnetic field, and the densities ρ_i and currents j_i^μ are bilinear combinations of Dirac spinors, namely $\bar{\psi}\Gamma_i\psi$ with $i = S,V,TV$ representing the symmetry of the coupling. The subscript S stands for isoscalar-scalar ($\Gamma_S = 1$), V for isoscalar-vector ($\Gamma_V = \gamma^\mu$), and TV for isovector-vector ($\Gamma_{TV} = \gamma^\mu t_3$) types of coupling characterized by their transformation properties in isospin and in space time.

In order to obtain the radial wave function given by Eq. (3) and the energy of hypernuclear low-lying states, we multiply $\langle\mathscr{F}_k^{JM}|$ to the total Schrödinger equation,

$\hat{H}|\Psi_{JM}\rangle = E_J|\Psi_{JM}\rangle$, and integrate it over $\hat{\boldsymbol{r}}$ and $\{\boldsymbol{r}_N\}$. This leads to the following coupled-channels equations:

$$\left(\frac{d}{dr} - \frac{\kappa-1}{r}\right)g_k(r) + (E_{I_n} - E_J)f_k(r) + \sum_{k'}\left[U_V^{kk'}(r) + U_S^{kk'}(r)\right]f_{k'}(r) = 0, \tag{9a}$$

$$\left(\frac{d}{dr} + \frac{\kappa+1}{r}\right)f_k(r) - \left(E_{I_n} - 2m_\Lambda - E_J\right)g_k(r) - \sum_{k'}\left[U_V^{kk'}(r) - U_S^{kk'}(r)\right]g_{k'}(r) = 0, \tag{9b}$$

where κ is defined as $\kappa = (-1)^{j+\ell+1/2}(j+1/2)$. With the multipole expansion for the δ function in coordinate space,

$$\delta(\boldsymbol{r}-\boldsymbol{r}') = \frac{\delta(r-r')}{rr'}\sum_{\lambda,\mu}Y_{\lambda\mu}(\hat{\boldsymbol{r}})Y^*_{\lambda\mu}(\hat{\boldsymbol{r}}'), \tag{10}$$

the vector and scalar coupling potentials in Eqs. (9a) and (9b) read

$$\begin{aligned} U_V^{kk'}(r) &\equiv \left\langle \mathscr{F}_k^{JM}\middle|\alpha_V^{N\Lambda}\sum_{i=1}^{A_c}\delta(\boldsymbol{r}-\boldsymbol{r}_{Ni})\middle|\mathscr{F}_{k'}^{JM}\right\rangle \\ &= (-1)^{j'+I+J}\sum_\lambda\langle j\ell||Y_\lambda||j'\ell'\rangle\begin{Bmatrix} J & I & j \\ \lambda & j' & I'\end{Bmatrix} \\ &\quad\times\alpha_V^{N\Lambda}\rho_{\lambda,V}^{I_nI_{n'}}(r), \end{aligned} \tag{11}$$

and

$$\begin{aligned} U_S^{kk'}(r) &\equiv \left\langle \mathscr{F}_k^{JM}\middle|\alpha_S^{N\Lambda}\sum_{i=1}^{A_c}\gamma_i^0\delta(\boldsymbol{r}-\boldsymbol{r}_{Ni})\middle|\mathscr{F}_{k'}^{JM}\right\rangle \\ &= (-1)^{j'+I+J}\sum_\lambda\langle j\ell||Y_\lambda||j'\ell'\rangle\begin{Bmatrix} J & I & j \\ \lambda & j' & I'\end{Bmatrix} \\ &\quad\times\alpha_S^{N\Lambda}\rho_{\lambda,S}^{I_nI_{n'}}(r), \end{aligned} \tag{12}$$

where $\rho_{\lambda,V}^{I_nI_{n'}}(r)$ and $\rho_{\lambda,S}^{I_nI_{n'}}(r)$ are the reduced vector and scalar transition densities defined, respectively, as

$$\rho_{\lambda,V}^{I_nI_{n'}}(r) = \left\langle\Phi_{I_n}\middle\|\sum_{i=1}^{A_c}\frac{\delta(r-r_{Ni})}{r_{Ni}r}Y_\lambda(\hat{\boldsymbol{r}}_{Ni})\middle\|\Phi_{I_{n'}}\right\rangle, \tag{13a}$$

$$\rho_{\lambda,S}^{I_nI_{n'}}(r) = \left\langle\Phi_{I_n}\middle\|\sum_{i=1}^{A_c}\gamma_i^0\frac{\delta(r-r_{Ni})}{r_{Ni}r}Y_\lambda(\hat{\boldsymbol{r}}_{Ni})\middle\|\Phi_{I_{n'}}\right\rangle, \tag{13b}$$

between the nuclear initial state $I_{n'}$ and the final state I_n. The detailed expression for the transition densities in the nonrelativistic multireference DFT framework has been derived in Ref. [30] by one of the present authors. The formalism has also been generalized to the relativistic case within a multireference CDFT (MR-CDFT) to study a "bubble" structure in light nuclei [31,32]. In this work, we extend this formalism to study low-lying states of hypernuclei.

With the radial wave function $\mathscr{R}_k(r)$ in the coupled-channels equations (9a) and (9b), one can compute the probability P_k of the channel k in the total wave function Ψ_{JM} as

$$P_k = \int r^2dr\,|\mathscr{R}_k(r)|^2 = \int r^2dr[|f_k(r)|^2 + |g_k(r)|^2]. \tag{14}$$

The wave function is normalized as $\sum_k P_k = 1$.

B. Projected potential energy surface

In order to apply the formalism presented in the previous subsection, one has to specify the core states Φ_{I_n}. A simple choice for this is to construct them as the projected mean-field states with the intrinsic deformation β

$$\left|\Phi_{IM_I}(\beta)\right\rangle = \hat{P}^I_{M_IK}\hat{P}^N\hat{P}^Z|\varphi(\beta)\rangle, \tag{15}$$

where the particle number projector $\hat{P}^{N_\tau}$ has the form

$$\hat{P}^{N_\tau} = \frac{1}{2\pi}\int_0^{2\pi}d\varphi_\tau e^{i\varphi_\tau(\hat{N}_\tau - N_\tau)}, \quad (\tau = n,p), \tag{16}$$

and the operator $\hat{P}^I_{M_IK}$ is the three-dimensional angular momentum projection operator given by

$$\hat{P}^I_{M_IK} = \frac{2I+1}{8\pi^2}\int d\Omega D^{I*}_{M_IK}(\Omega)\hat{R}(\Omega). \tag{17}$$

Here, Ω represents a set of Euler angles (ϕ,θ,ψ), and the measure is $d\Omega = d\phi\sin\theta d\theta d\psi$. $\hat{R}(\Omega)$ and $D^I_{M_IK}(\Omega)$ are the rotation operator and the Wigner D function, respectively [33]. In Eq. (15), the wave function $|\varphi(\beta)\rangle$ is a Slater determinant of quasiparticle states with quadrupole deformation β generated with the constrained relativistic mean-field (RMF) calculation. For simplicity, in this paper we consider only the axial deformation for the nuclear core and thus the K quantum number is zero in Eq. (15).

In this approach, the hypernuclear states Ψ_{JM} are given for each deformation β. This allows one to construct the projected energy surface for hypernuclei. That is, one can define the total energy $E_J(\beta)$ by taking $\langle\Psi_{JM}|\hat{H}|\Psi_{JM}\rangle$ at each deformation β and for each spin-parity, J^π. Notice that the coupled-channels equations (9a) and (9b) are solved at each deformation, and thus the effect of core excitations is taken into account in the projected energy surface so obtained.

C. Multireference covariant density functional for nuclear core states and transition densities

One can improve the calculations in the previous subsection by using Φ_{I_n} from the MR-CDFT calculation in the context of generator coordinate method (GCM) [34–36], that is,

$$\left|\Phi_{I_nM_I}\right\rangle = \sum_\beta F_n^I(\beta)\hat{P}^I_{M_IK}\hat{P}^N\hat{P}^Z|\varphi(\beta)\rangle. \tag{18}$$

In this wave function, a set of Slater determinants with different quadrupole deformation β is superposed according to the idea of GCM. The weight function $F_n^I(\beta)$ in the wave function (18) is determined by requiring that the energy expectation value is stationary with respect to an arbitrary variation of $F_n^I(\beta)$, which leads to the Hill-Wheeler-Griffin (HWG)

equation [37],

$$\sum_{\beta'}[\mathscr{H}^I(\beta,\beta') - E_{I_n}\mathscr{N}^I(\beta,\beta')]F_n^I(\beta') = 0. \quad (19)$$

Here, $\mathscr{N}^I(\beta,\beta') = \langle\varphi(\beta)|\hat{P}^I_{00}\hat{P}^N\hat{P}^Z|\varphi(\beta')\rangle$ and $\mathscr{H}^I(\beta,\beta') = \langle\varphi(\beta)|\hat{H}\hat{P}^I_{00}\hat{P}^N\hat{P}^Z|\varphi(\beta')\rangle$ are the norm and the energy kernels, respectively. In the calculations, the energy overlap in the energy kernel is taken to be the same functional form as in the nuclear mean-field energy, but replacing the densities and currents with mixed ones, that is, off-diagonal components of the density and current matrices [34–36].

Since the projected mean-field states do not form an orthogonal basis and the weights $F_n^I(\beta)$ in Eq. (18) are not orthogonal functions, it is convenient to construct a set of orthonormal collective wave functions g_n^I as [38]

$$g_n^I(\beta) = \sum_{\beta'}[\mathcal{N}^I]^{1/2}(\beta,\beta')F_n^I(\beta'). \quad (20)$$

Notice that the modulus square of $g_n^I(\beta)$ does not represent the probability to find the deformation β in the GCM state. For the axial symmetric case, however, $g_n^I(\beta)$ provides a good indication about the dominant configurations in the collective states.

With the GCM wave functions for $|\Phi_{I_n}\rangle$, one can calculate the reduced vector transition density in Eq. (13a) as follows [30]:

$$\rho^{I_n I'_{n'}}_{\lambda,V}(r) = (-1)^{I'-I}\frac{\hat{I}^2}{\hat{I}'}\sum_{\beta,\beta'}F_n^{I*}(\beta)F_{n'}^{I'}(\beta')\sum_{K\nu}\langle I0\lambda\nu|I'0\rangle \times\int d\hat{\mathbf{r}}Y^*_{\lambda\nu}(\hat{\mathbf{r}})\langle\varphi(\beta)|\hat{\rho}_V(\mathbf{r})\hat{P}^{I'}_{0K}\hat{P}^N\hat{P}^Z|\varphi(\beta')\rangle, \quad (21)$$

where the notation $\hat{I} = \sqrt{2I+1}$ is introduced for simplicity, and the vector density operator is defined as follows:

$$\hat{\rho}_V(\mathbf{r}) = \sum_{i=1}^{A_c}\delta(\mathbf{r}-\mathbf{r}_{Ni}). \quad (22a)$$

The reduced scalar density in Eq. (13b) can also be expressed in a similar way.

D. Electric quadrupole transition strengths between hypernuclear states

The electric quadrupole ($E2$) transition strength from an initial state $|J_i\rangle$ to a final state $|J_f\rangle$ in Λ hypernuclei is defined as

$$B(E2;J_i\to J_f) = \frac{1}{2J_i+1}|\langle J_f||\hat{Q}_2||J_i\rangle|^2. \quad (23)$$

Here, the $E2$ operator reads $\hat{Q}_{2\mu} = \sum_{i\in p}r_i^2Y_{2\mu}(\hat{r}_i)$. Substituting the wave function for the hypernuclear states, Eq. (1), in this equation, one finds the reduced matrix element to be

$$\langle J_f||\hat{Q}_2||J_i\rangle = \sum_{k_i,k_f}\int drr^2\mathscr{R}^\dagger_{k_f}(r)\mathscr{R}_{k_i}(r)\left\langle\mathscr{F}^{J_f}_{k_f}\middle\|\hat{Q}_2\middle\|\mathscr{F}^{J_i}_{k_i}\right\rangle \quad (24)$$

with

$$\left\langle\mathscr{F}^{J_f}_{k_f}\middle\|\hat{Q}_2\middle\|\mathscr{F}^{J_i}_{k_i}\right\rangle = \delta_{j_fj_i}\delta_{\ell_f\ell_i}(-1)^{I_f+j_i+J_i}\hat{J}_i\hat{J}_f\begin{Bmatrix}I_f & J_f & j_i\\ J_i & I_i & 2\end{Bmatrix}\langle I_{n_f}\|\hat{Q}_2\|I_{n_i}\rangle \quad (25)$$

(see Eq. (7.1.8) in Ref. [33]). Here, $\langle I_{n_f}||\hat{Q}_2||I_{n_i}\rangle$ is the reduced $E2$ transition matrix element between the nuclear core states $|I_f,n_f\rangle$ and $|I_i,n_i\rangle$ and it is related to the proton vector transition density in Eq. (21) as

$$\langle I_{n_f}\|\hat{Q}_2\|I_{n_i}\rangle = \hat{I}_i\int drr^4\rho^{I_{n_f}I_{n_i}}_{2,V}(r). \quad (26)$$

III. RESULTS AND DISCUSSION

We now numerically solve the coupled-channels equations and discuss low-lying spectrum of hypernuclei. The procedure of the calculations and the numerical details are listed as follows.

(i) Self-consistent deformation constrained RMF+BCS calculation for the nuclear core states. This step is to generate a set of deformed states $|\varphi(\beta)\rangle$ with different quadrupole deformation β. The Dirac equation for nucleons is solved with the basis of a three-dimensional harmonic oscillator (3DHO) with $N_{\rm sh} = 10$ major shells for ^{12}C and ^{20}Ne, and with $N_{\rm sh} = 12$ for ^{154}Sm. The oscillator length parameter in the 3DHO is chosen as $b_x = b_y = b_z = \sqrt{\hbar/m\omega_0}$, where m is the nucleon mass and the oscillator frequency is determined to be $\hbar\omega_0 = 41A_c^{-1/3}$ MeV. In the most of calculations shown below, we employ the nonlinear point-coupling EDF with the PC-F1 [29] set for the particle-hole channel, although we also use the PC-PK1 set [39] for ^{20}Ne in order to study the parameter set dependence. In these energy density functionals, a density-independent δ force is used for the particle-particle channel, supplemented with an energy-dependent cutoff for the pairing active space [40].

(ii) MR-CDFT calculation for the low-lying states of nuclear core. This step is to obtain the wave functions Φ_{I_n} for the core state I_n. The mean-field wave functions are projected onto good particle numbers (N,Z) and angular momentum I, which form a set of nonorthogonal basis. The Gauss-Legendre quadrature is used for integrals over the Euler angle θ in the calculations of the norm and Hamiltonian kernels. For the ^{12}C nucleus, the number of mesh points in the interval $[0,\pi]$ for θ is chosen to be 14. The number of gauge angle φ for the particle number projection is chosen to be 7. For ^{20}Ne and ^{154}Sm, we use the mesh points of 16 and 9 for the angular momentum and the particle number projections, respectively. The energy and wave function of the core state I_n are determined by solving the HWG equation, Eq. (19) [34–38]. With the wave functions of nuclear core states, one can calculate the transition densities which are used to determine the coupling potentials in the coupled-channels equations.

(iii) Coupled-channels calculation for the low-lying states of Λ hypernuclei. With the coupling potentials so obtained, the coupled-channels equations are solved by expanding the radial wave function $\mathscr{R}_{j\ell I_n}(r)$ on the basis of eigenfunctions of a spherical harmonic oscillator with 18 major shells. From the solutions of the coupled-channels equations, we construct the

spectrum of hypernucleus and calculate the $B(E2)$ transition strengths.

A. Application to $^{13}_{\Lambda}$C

1. Properties of the core states

We first apply the method to $^{13}_{\Lambda}$C. Figure 2 shows the energy curves for the core nucleus, ^{12}C. The dotted line is obtained in the mean-field approximation, while the other lines show the projected energy surface for each angular momentum I. The mean-field energy curve exhibits a pronounced minimum at the spherical configuration with a steep rise with deformation β, as expected for a nucleus with large neutron and proton shell gaps. The energy gained from restoration of rotational symmetry increases with deformation β and together with the particle number projection the location of energy minimum is shifted on the curve. The minimum of the energy curve with 0^+ is found on the oblate side with $\beta = -0.3$. Besides, the second minimum appears around $\beta = 2.4$ in the mean-field energy curve, which is shifted to $\beta = 2.7$ in the projected energy curve for $I^\pi = 0^+$. It has been shown that the configuration for this minimum has a 3α linear-chain structure [41].

After mixing the projected mean-field configurations, one obtains the energies of low-lying states (see the filled squares in Fig. 2). The wave function of these states is displayed in Fig. 3 for the lowest three states with $I = 0,2,4$, and 6. The ground state of ^{12}C is dominated by the spherical configuration. The collective wave functions and the energy spectrum indicate that there is a coexistence of an anharmonic spherical vibrator and an oblate deformed band at low excitation energies of ^{12}C. Both structures are not pure and distorted by their strong mixing. The high-lying $0_3^+, 2_3^+$, and 4_2^+ states seem to form a rotational band dominated by the 3α-linear configuration, in which the collective wave functions are much extended

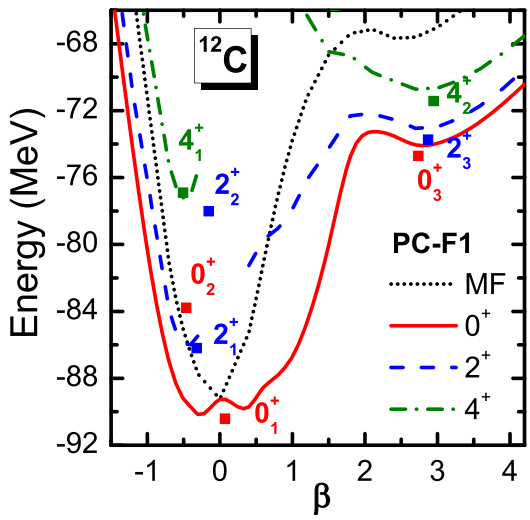

FIG. 2. (Color online) The energy curve of the mean-field state and the particle-number and angular momentum projected ($I^\pi = 0^+, 2^+$, and 4^+) states for ^{12}C as a function of the intrinsic quadrupole deformation β. The filled squares indicate the lowest three GCM solutions for each I^π, which are plotted at their average deformation $\bar{\beta} \equiv \sum_\beta |g_n^I(\beta)|^2 \beta$, where $g_n^I(\beta)$ is the collective wave functions defined by Eq. (20). The results are obtained with the PC-F1 force.

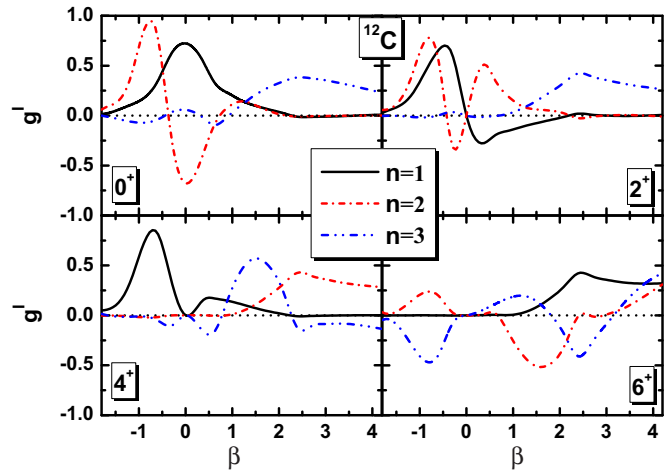

FIG. 3. (Color online) The collective wave functions g_n^I given by Eq. (20), for the first three states in ^{12}C with spin parities of $0^+, 2^+, 4^+$, and 6^+.

to a large deformation region. A similar rotational band corresponding to a 4α-linear configuration has also been found in the high-lying states of ^{16}O [42].

Figure 4 shows the vector and scalar transition densities $\rho_\lambda^{0\lambda}$ in the low-lying yrast states ($n = 1$) of ^{12}C, where the multipolarity λ is taken as 0,2, and 4. $\rho_0^{00}(r)$ is nothing but the total nucleon density for the 0_1^+ ground state multiplied by a factor $\sqrt{4\pi}$. It is shown that the transition density $\rho_\lambda^{0\lambda}$ decreases by one order of magnitude as λ increases from 0 to 2 and from 2 to 4. Besides, we also plot the transition densities ρ_λ^{22} with $\lambda = 0,2$, and 4, ρ_λ^{24} with $\lambda = 2,4$, and 6, and ρ_λ^{26} with $\lambda = 4,6$, and 8. Notice that the vector and scalar transition densities are slightly different from one another.

The convolution of the proton vector transition densities in Fig. 4 with a Gaussian form factor for a finite proton size yields the charge transition densities, $\rho_{L,\mathrm{ch}}^{I_n I'_{n'}}(r)$, which are related to the form factor $F_L(q)$ for electron scattering with an angular momentum transfer L by the following relation [30]:

$$F_L(q) = \frac{\sqrt{4\pi}}{Z} \int_0^\infty dr r^2 \rho_{L,\mathrm{ch}}^{I_n I'_{n'}}(r) j_L(qr), \qquad (27)$$

where $j_L(qr)$ is the spherical Bessel function. The coefficient $\sqrt{4\pi}/Z$ is chosen so that the elastic part of the form factor $F_0(q)$ is unity at $q = 0$. A comparison of our results with the data is shown in Fig. 5. One can see that the form factors $F_L(q)$ are in rather good agreement with the data except for the underestimation of the elastic form factor after the first minimum, as was found also in the recent studies for ^{12}C [45] and ^{24}Mg [30] based on the Skyrme forces. This may be because the spreading of the collective wave function in quadrupole deformation space is somewhat overestimated in the calculations, decreasing the weights of the large-q components of the transition density [30,45]. In fact, the charge radius of ^{12}C by the present GCM calculation is 2.57 fm, which is larger than the empirical value of 2.47 fm [46].

Figure 6 shows the charge form factors for the interband transitions between the two bands with $n = 1$ and $n = 2$

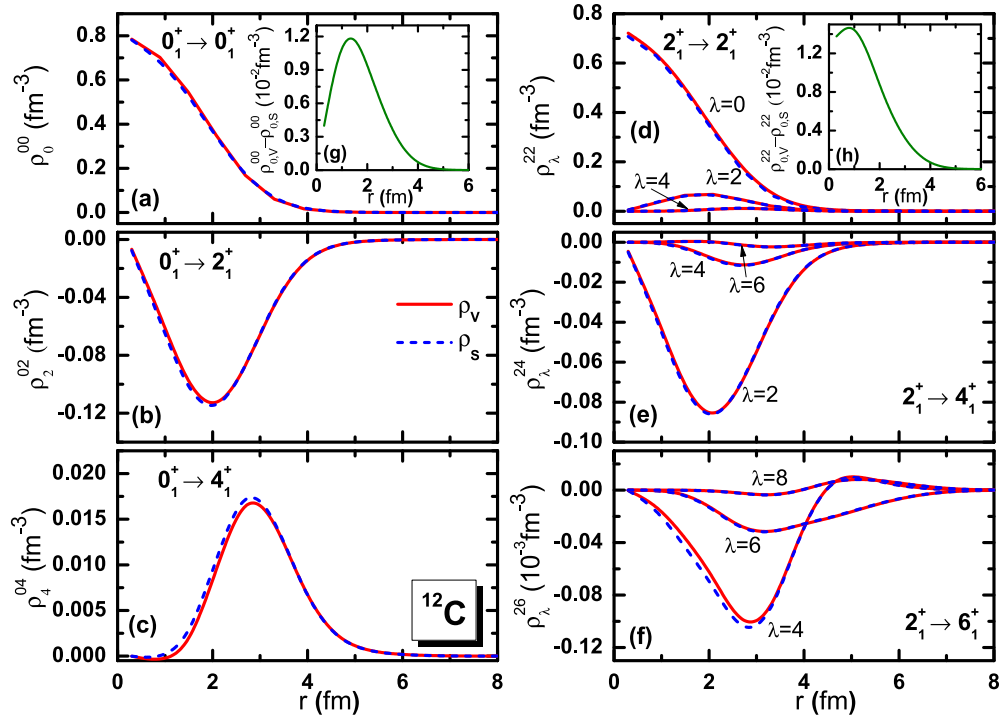

FIG. 4. (Color online) The vector transition density, $\rho^{I_n,I'_n}_{\lambda,V}$, given by Eq. (13a), and the scalar transition density, $\rho^{I_n,I'_n}_{\lambda,S}$, given by Eq. (13b), in the low-lying states ($n = 1$) of ^{12}C. These are plotted by the solid and the dashed lines, respectively. The insets show the difference of the vector and scalar transition densities.

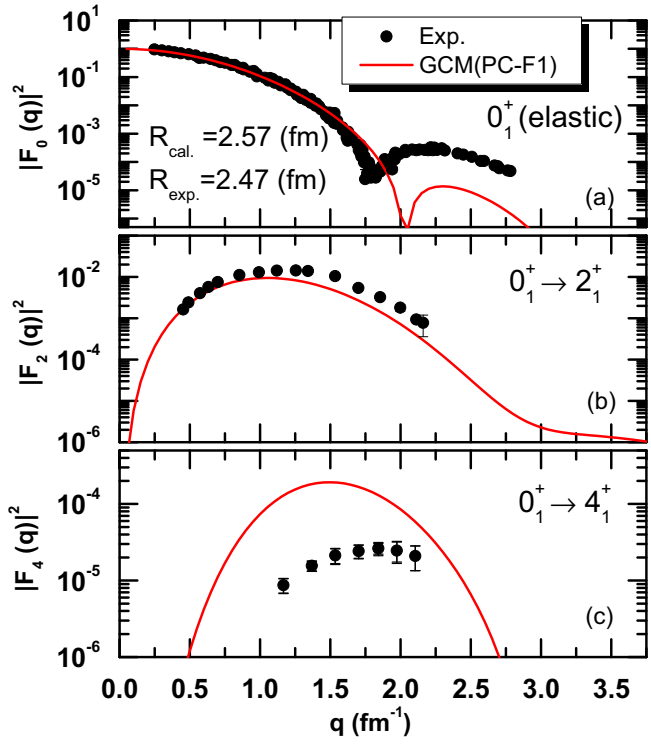

FIG. 5. (Color online) The charge form factor for the transition from the ground state to (a) the ground state, (b) the excited 2_1^+ state, and (c) the excited 4_1^+ state in ^{12}C calculated with the GCM method with the PC-F1 force, in comparison with the available data [43,44]. R on the top panel is the root-mean-square charge radius of ^{12}C.

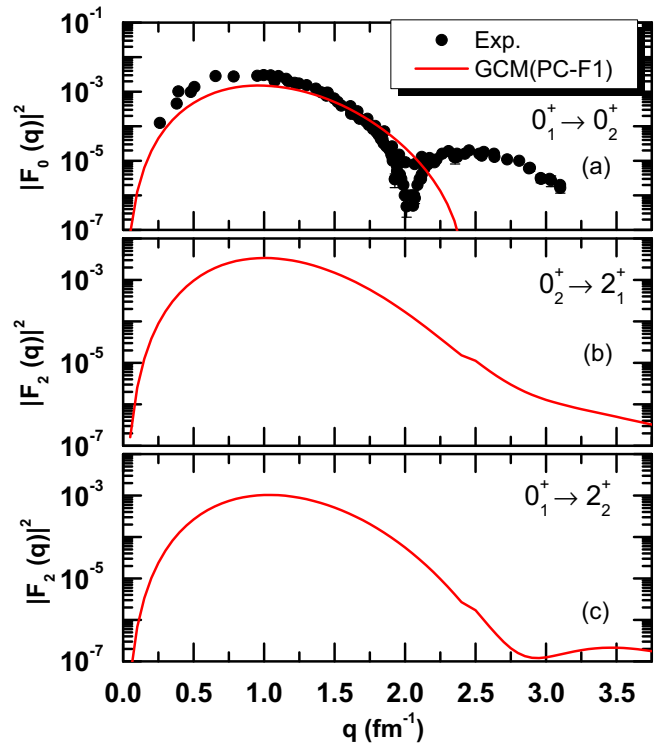

FIG. 6. (Color online) The charge form factors between the two bands with $n = 1$ and $n = 2$ in ^{12}C calculated with the GCM method with the PC-F1 force, in comparison with the available data from Ref. [47].

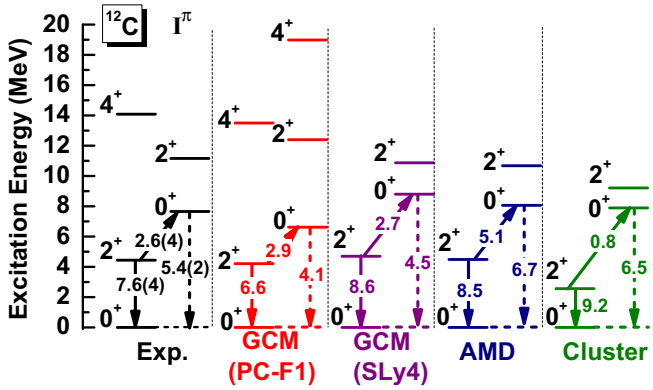

FIG. 7. (Color online) The spectrum of ^{12}C obtained with several methods, that is, the GCM with the PC-F1 interaction (the present calculation), GCM with the Skyrme SLy4 force [45], antisymmetrized molecular dynamics (AMD) [48], and the α cluster model [47]. The excitation energies are given in units of MeV. The solid and the dashed arrows are the quadrupole transition strength $B(E2)$ (e^2 fm^4) and the electric monopole transition matrix element $|M(E0)|$ (e fm^2), respectively. The experimental data are taken from Refs. [50,51].

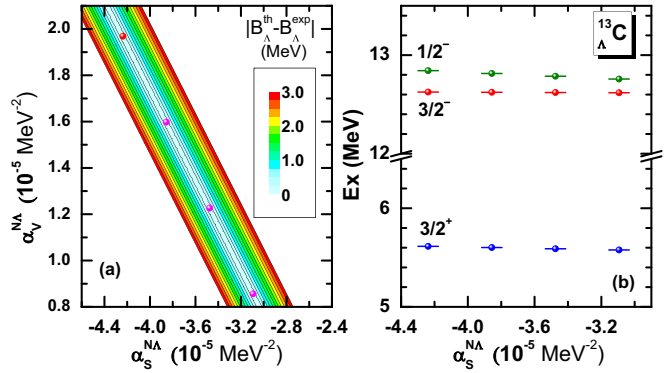

FIG. 8. (Color online) (a) A contour plot of the absolute value of the difference between the theoretical and the experimental hyperon binding energies of $^{13}_\Lambda$C hypernucleus as a function of the coupling strength parameters $\alpha_S^{N\Lambda}$ and $\alpha_V^{N\Lambda}$ in the $N\Lambda$ interaction. The calculated energies are obtained with the microscopic particle-rotor model. (b) Energy levels of the $3/2^+$, $3/2^-$, and $1/2^-$ states in $^{13}_\Lambda$C calculated with the strength parameters denoted by the dots in the panel (a).

in ^{12}C. Since the 0_2^+ state is the Hoyle state with dilute 3α structure, which is beyond the model space of the present calculation, the inelastic form factor $F_0(q)$ corresponding to the transition from the 0_1^+ to the 0_2^+ states is significantly underestimated in the high-q region beyond the first minimum. It is worthwhile to mention that the calculated electric monopole transition matrix element $|M(E0: 0_2^+ \to 0_1^+)| = 4.1\ e\text{fm}^2$ and the charge radius of 0_2^+ (2.73 fm) are in good agreement with the results ($4.5 \pm 0.2\ e\text{fm}^2$ and 2.73 ± 0.02 fm, respectively) of the recent configuration mixing calculation based on a Skyrme force [45]. These values should be compared with the data $|M(E0: 0_2^+ \to 0_1^+)| = 5.4(2)\ e\text{fm}^2$ and the charge radius from other calculations for the Hoyle state, such as 3.27 fm by the antisymmetrized molecular dynamics [48], 3.38 fm by the fermionic molecular dynamics [47], and 3.83 fm by the α-condensation model [49].

The low-lying spectrum of ^{12}C with MR-CDFT calculation is shown in Fig. 7, in which the results are compared with the experiment data [50,51] as well as with other model calculations [45,47,48]. One can see that the low-lying spectrum is reproduced rather well by the present calculation, although the excitation energies are systematically overestimated. The electric monopole transition matrix element $|M(E0)|$ and the quadrupole transition strength $B(E2)$ are also in good agreement with the data and the other model calculations.

2. ΛN interaction

The core states obtained in the previous subsection are used as inputs for the coupled-channels calculations for the hypernucleus $^{13}_\Lambda$C. To this end, the parameters $\alpha_S^{N\Lambda}$ and $\alpha_V^{N\Lambda}$ in the $N\Lambda$ interaction, Eqs. (6) and (7), are fitted with the microscopic particle-rotor model to the experimental Λ binding energy of $^{13}_\Lambda$C, that is, $B_\Lambda^{(\text{exp.})} = 11.38 \pm 0.05$ MeV [1]. Figure 8(a) shows a contour plot of the absolute value of the difference between the theoretical and the experimental hyperon binding energies as a function of $\alpha_S^{N\Lambda}$ and $\alpha_V^{N\Lambda}$. This is obtained by including in Eq. (1) the core states up to $n_{\text{cut}} = 2$ and $I_{\text{cut}} = 4$. Obviously, the two strength parameters cannot be uniquely determined by fitting only to B_Λ and are linearly correlated as illustrated in Fig. 8(a).

Taking a few sets of the parameters along the valley with $B_\Lambda^{\text{th}} = B_\Lambda^{\text{exp}}$ in Fig. 8(a), we calculate the energy of each of the low-lying excited states of $3/2^+$, $3/2^-$, and $1/2^-$ in $^{13}_\Lambda$C [see Fig. 8(b)]. One can see that the excitation energies of $3/2^+$, $3/2^-$ depend on the choice of the parameters only weakly. The energy of $1/2^-$ state slightly decreases with the decrease of the absolute value of the coupling strengths. For all the sets of the parameters ($\alpha_S^{N\Lambda}$,$\alpha_V^{N\Lambda}$) in the region of concerned, the energy splitting between the first $1/2^-$ and $3/2^-$ states is in agreement with the data $152 \pm 54(\text{stat}) \pm 36(\text{syst})$ keV [53,54]. Therefore, as one of the choices, we first fix the value of $\alpha_S^{N\Lambda}$ to be -4.2377×10^{-5} MeV^{-2}, which is the same value as in the PCY-S2 set [28], and determine $\alpha_V^{N\Lambda}$ to be 1.969×10^{-5} MeV^{-2}. With this parameter set for the ΛN interaction, the energy splitting between the $1/2^-$ and $3/2^-$ states is 198.9 keV.

3. Projected potential energy surface

With the $N\Lambda$ interaction determined in the previous subsection, let us first investigate the projected potential energy surface for $^{13}_\Lambda$C. Figure 9 shows the resultant energy $E_J(\beta)$ for the $J^\pi = 1/2^+$, $1/2^-$, and $3/2^-$ states in $^{13}_\Lambda$C as a function of the deformation β of the core nucleus. These are obtained by solving the coupled-channels equations for each β. For comparison, the figure also shows the potential energy curve in the single-channel calculations without taking into account the core excitations (the dot-dashed lines) as well as those for the core nucleus (the dashed lines). The energy surfaces obtained with the coupled-channel calculations are systematically lower than that with the single-channel calculation due to the additional configuration mixing effect. One can see that the

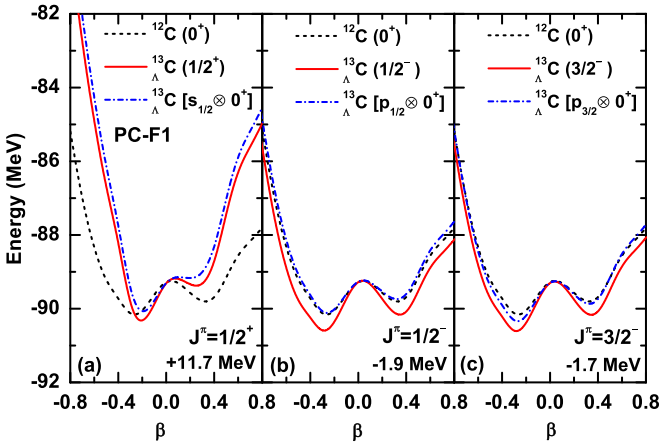

FIG. 9. (Color online) The potential energy surfaces of hypernucleus $^{13}_{\Lambda}$C obtained with the single-channel calculation (the dot-dashed lines) and the coupled-channel calculation (the solid lines) with spin parity of (a) $J^{\pi} = 1/2^{+}$, (b) $J^{\pi} = 1/2^{-}$, and (c) $J^{\pi} = 3/2^{-}$ as a function of deformation parameter β. For comparison, the figure also shows the energy surface for the nuclear core with spin-parity of $I^{\pi} = 0^{+}$ (the dashed lines). The energy surfaces for hypernuclei are shifted by a constant amount as indicated in each panel.

hypernuclear energy curve with spin parity of $1/2^{+}$ has an oblate minimum with $|\beta|$ significantly smaller than that of ^{12}C with 0^{+}, indicating a smaller collectivity. On the other hand, for $J^{\pi} = 1/2^{-}$, the deformation around the oblate minimum is similar to that of ^{12}C, but with a higher barrier at the spherical shape. This leads to a smaller effect of shape mixing between the prolate and oblate configurations and thus a larger average deformation in $^{13}_{\Lambda}$C. The main component of the $1/2^{+}$ and $1/2^{-}$ hypernuclear states are the Λ particle in $s_{1/2}$ and $p_{1/2}$ orbits coupled to the ground state of ^{12}C, respectively. It implies that a Λ particle in the s (p) orbit decreases (increases) the collectivity of ^{12}C, which is consistent with the findings in the recent studies [14,23].

4. Single-channel calculations

Let us now employ the core states described with the GCM method and discuss the spectrum of $^{13}_{\Lambda}$C. Before we present the results of full coupled-channels calculations, we first discuss the results of single-channel calculations, restricting the Λ-hyperon to a specific orbital coupled to a single core state. In this case, we take only the diagonal component in the coupling potentials, Eqs. (11) and (12), in the coupled-channels equations. The coupled-channels equations are then simplified as

$$\left(\frac{d}{dr} - \frac{\kappa - 1}{r}\right) g_k(r) + \left(E_{I_n} - E_J\right) f_k(r) + \left[U_V^{kk}(r) + U_S^{kk}(r)\right] f_k(r) = 0, \tag{28}$$

$$\left(\frac{d}{dr} + \frac{\kappa + 1}{r}\right) f_k(r) - \left(E_{I_n} - 2m_{\Lambda} - E_J\right) g_k(r) - \left[U_V^{kk}(r) - U_S^{kk}(r)\right] g_k(r) = 0. \tag{29}$$

The results for the Λ particle in the $s_{1/2}$, $p_{1/2}$, and $p_{3/2}$ orbitals are shown in the columns (d)–(g) of Fig. 10. For comparison, the figure also shows the spectrum of the core nucleus ^{12}C in Figs. 10(a)–10(c) (these are actually the same as those in Fig. 7). A $\Lambda_{\ell j}$ hyperon coupled to the core state with angular momentum I^{+} produces several hypernuclear states with J^{π}, with the total angular momentum J running from $J = |I - j|$ to $J = I + j$, with the parity of $\pi = (-1)^{\ell}$. When the Λ particle is restricted to the $s_{1/2}$ orbit, a doublet states with $(I - 1/2)^{+}$ and $(I + 1/2)^{+}$ are yielded, which are degenerate in energy for $I > 0$. On the other hand, a spectrum is more complex for the case of Λ particle in the $p_{3/2}$ orbital.

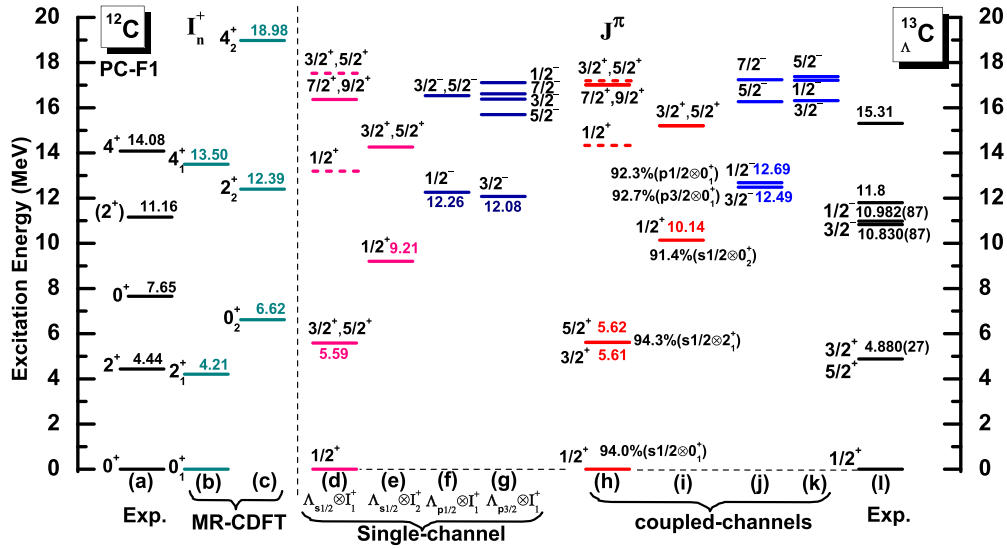

FIG. 10. (Color online) The low-energy excitation spectra of ^{12}C [(a)–(c)] and $^{13}_{\Lambda}$C [(d)–(l)]. For ^{12}C, the full GCM calculations are compared with the experimental data taken from Ref. [52]. The columns (h) and (i) show the positive-parity states in $^{13}_{\Lambda}$C, while the columns (j) and (k) show the negative-parity states. The experimental data of $^{13}_{\Lambda}$C are taken from Refs. [53,54]. For comparison, the results of single-channel calculation for $^{13}_{\Lambda}$C with the Λ particle in the $s_{1/2}$, $p_{1/2}$ and $p_{3/2}$ orbitals are also plotted in the columns (d)–(g).

In this case, the multiplet states with $J \in [|I-j|,(I+j)]$ are ordered according to the properties of the coupling potential in Eq. (28).

For instance, in the case of $\Lambda_{p3/2} \otimes 2_1^+$, the multiplets are ordered as $5/2^-,3/2^-,7/2^-$, and $1/2^-$ [see Fig. 10(g)]. In order to understand this, we write the coupling potentials for the configuration k as

$$U_m^{kk} = (-1)^{j+I+J} \sum_\lambda \langle j\ell||Y_\lambda||j\ell\rangle \begin{Bmatrix} J & I & j \\ \lambda & j & I \end{Bmatrix} \alpha_m^{N\Lambda} \rho_{\lambda,m}^{I_n I_n}$$
$$\equiv C_0 \sum_\lambda C_{1\lambda} C_{2\lambda} \alpha_m^{N\Lambda} \rho_{\lambda,m}^{I_n I_n}, \quad (30)$$

where the indices $m = S$ and V represent the scalar and vector potentials, respectively. The coefficients $C_n (n = 0,1,$ and $2)$ are defined as $C_0 \equiv (-1)^{j+I+J}$,

$$C_{1\lambda} \equiv \langle j\ell||Y_\lambda||j\ell\rangle = \frac{(-1)^{j+1/2}}{\sqrt{4\pi}} \hat{j}^2 \hat{\lambda} \begin{pmatrix} j & \lambda & j \\ 1/2 & 0 & -1/2 \end{pmatrix} \delta_{\lambda,even}, \quad (31)$$

and

$$C_{2\lambda} \equiv \begin{Bmatrix} J & I & j \\ \lambda & j & I \end{Bmatrix}. \quad (32)$$

Table I lists the value of each of the coefficients C_n. The transition densities $\alpha_m^{N\Lambda}\rho_{\lambda,m}^{22}(r)$ and the potential $U_V^{kk}(r) + U_S^{kk}(r)$ with $k \equiv (j,\ell,I_n) = (\frac{3}{2},1,2_1)$ are displayed in Fig. 11 as a function of radial coordinate r. It is seen that the potential $U_V^{kk}(r) + U_S^{kk}(r)$ becomes gradually deeper in the order of $J^\pi = 1/2^-,7/2^-,3/2^-,5/2^-$, which is consistent with the distribution of energy levels of these multiplets. It is seen in Table I that the product $C_0 C_{1\lambda} C_{2\lambda}$ is the same among the multiplets for $\lambda = 0$, and thus the origin for the energy difference among these four hypernuclear states is the nonzero $\lambda = 2$ term in the potential (30). That is, the splitting of $J^\pi = 1/2^-,7/2^-,3/2^-$, and $5/2^-$ hypernuclear states is originated from the nonzero transition density $\rho_2^{22}(r)$ [cf. Fig. 11(a)] due to the reorientation effect (that is, the transition between the same state) of 2_1^+ state in the deformed shape of ^{12}C. Since $\alpha_m^{N\Lambda}\rho_{\lambda,m}^{22}(r)$ is negative as shown in Fig. 11(a), the potential is most attractive for $J^\pi = 5/2^-$, which has a positive $C_0 C_{12} C_{22}$.

TABLE I. The coefficients in the potential for the $[\Lambda_{lj} \otimes 2^+]^{(J)}$ configurations [see Eqs. (31) and (32)].

$[\Lambda_{lj} \otimes 2^+]$	J^π	C_0	C_{20}	$C_0C_{10}C_{20}$	C_{22}	$C_0C_{12}C_{22}$
$[\Lambda_{p3/2} \otimes 2^+]$	$1/2^-$	1.00	$\frac{1}{\sqrt{20}}$	$\frac{1}{\sqrt{20\pi}}$	$\frac{\sqrt{14}}{20}$	$-\frac{\sqrt{14/\pi}}{20}$
$[\Lambda_{p3/2} \otimes 2^+]$	$3/2^-$	-1.00	$-\frac{1}{\sqrt{20}}$	$\frac{1}{\sqrt{20\pi}}$	0.00	0.00
$[\Lambda_{p3/2} \otimes 2^+]$	$5/2^-$	1.00	$\frac{1}{\sqrt{20}}$	$\frac{1}{\sqrt{20\pi}}$	$-\frac{\sqrt{14}}{28}$	$\frac{\sqrt{14/\pi}}{28}$
$[\Lambda_{p3/2} \otimes 2^+]$	$7/2^-$	-1.00	$-\frac{1}{\sqrt{20}}$	$\frac{1}{\sqrt{20\pi}}$	$-\frac{\sqrt{14}}{70}$	$-\frac{\sqrt{14/\pi}}{70}$
$[\Lambda_{p1/2} \otimes 2^+]$	$3/2^-$	1.00	$\frac{1}{\sqrt{10}}$	$\frac{1}{\sqrt{20\pi}}$	0.00	0.00
$[\Lambda_{p1/2} \otimes 2^+]$	$5/2^-$	-1.00	$-\frac{1}{\sqrt{10}}$	$\frac{1}{\sqrt{20\pi}}$	0.00	0.00

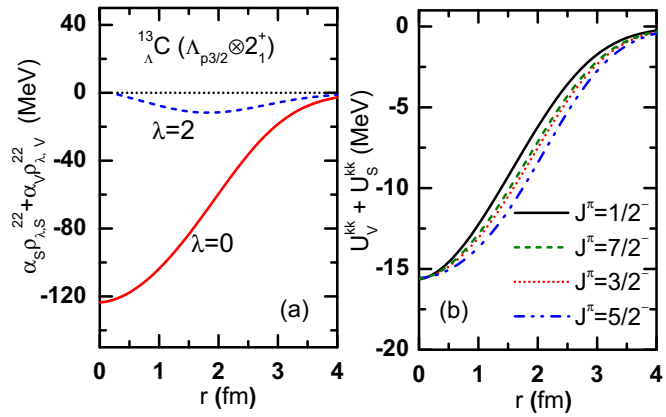

FIG. 11. (Color online) (a) The transition densities $\alpha_V \rho_{\lambda,V}^{22} + \alpha_S \rho_{\lambda,S}^{22}$ ($\lambda = 0$ and $\lambda = 2$) and (b) the potential $U_V^{kk}(r) + U_S^{kk}(r)$ in Eq. (28) for the hypernuclear states $J = 1/2^-,3/2^-,5/2^-,7/2^-$ with the $\Lambda_{p3/2} \otimes 2_1^+$ configuration as a function of the radial coordinate r.

For the configuration with Λ in $p_{1/2}$ orbital coupled to the nuclear core 2_1^+ state, the resultant doublet states $3/2^-$ and $5/2^-$ are degenerate in energy, since the coefficient $C = C_0 C_{1\lambda} C_{2\lambda}$ is not zero only for $\lambda = 0$, having the same value of $1/\sqrt{20\pi}$ between those two states (see Table I).

5. Coupled-channels calculations

Let us now solve the coupled-channels equations for $^{13}_{\Lambda}$C. To this end, we first examine the convergence feature of the excitation energies with respect to the cutoff of core states $n_{\rm cut}$ and the core angular momentum $I_{\rm cut}$. Figure 12 shows that $n_{\rm cut} = 2$ and $I_{\rm cut} = 4$ yield a good convergence for the low-

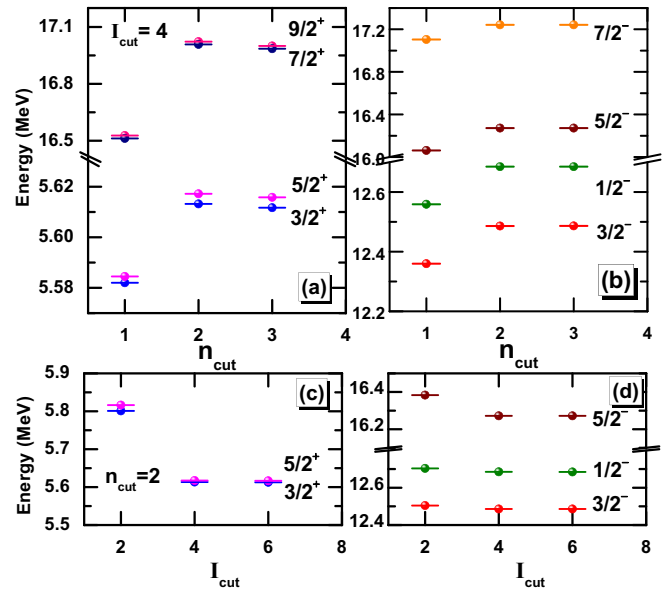

FIG. 12. (Color online) Excitation energy of low-lying states in $^{13}_{\Lambda}$C as a function of the cutoff of core states n [(a) and (b)] and the cutoff of core angular momentum I [(c) and (d)] for the coupled-channels calculations.

TABLE II. The probability P_{jlI_n} for the dominant components in the wave function for low-lying states of $^{13}_{\Lambda}$C obtained by the microscopic particle-rotor model. Only those components which have P_{jlI_n} larger than 0.1 are shown. E is the energy of each state obtained by solving the coupled-channels equations, while $E^{(0)}_{\rm 1ch}$ is the unperturbed energy obtained with the single-channel calculations. The energies are listed in units of MeV.

J^π	E	$(lj)\otimes I^\pi_n$	P_{jlI_n}	$E^{(0)}_{\rm 1ch}$
$1/2^+_1$	0.00	$s_{1/2}\otimes 0^+_1$	0.94	0.00
$3/2^+_1$	5.61	$s_{1/2}\otimes 2^+_1$	0.94	5.59
$5/2^+_1$	5.62	$s_{1/2}\otimes 2^+_1$	0.94	5.59
$7/2^+_1$	17.01	$s_{1/2}\otimes 4^+_1$	0.98	16.37
$9/2^+_1$	17.02	$s_{1/2}\otimes 4^+_1$	0.98	16.37
$1/2^+_2$	10.14	$s_{1/2}\otimes 0^+_2$	0.91	9.21
$3/2^+_2$	15.20	$s_{1/2}\otimes 2^+_2$	0.90	14.26
$5/2^+_2$	15.21	$s_{1/2}\otimes 2^+_2$	0.90	14.26
$1/2^-_1$	12.69	$p_{1/2}\otimes 0^+_1$	0.92	12.26
$3/2^-_1$	12.49	$p_{3/2}\otimes 0^+_1$	0.93	12.08
$5/2^-_1$	16.27	$p_{3/2}\otimes 2^+_1$	0.82	15.70
		$p_{1/2}\otimes 2^+_1$	0.17	16.53
$7/2^-_1$	17.24	$p_{3/2}\otimes 2^+_1$	0.97	16.62
$1/2^-_2$	17.22	$p_{1/2}\otimes 0^+_1$	0.60	17.36
		$p_{3/2}\otimes 2^+_1$	0.38	17.11
$3/2^-_2$	16.32	$p_{3/2}\otimes 2^+_1$	0.54	16.39
		$p_{1/2}\otimes 2^+_1$	0.45	16.53
$5/2^-_2$	17.38	$p_{1/2}\otimes 2^+_1$	0.80	16.53
		$p_{3/2}\otimes 2^+_1$	0.17	15.70

lying excited states, and we use these cutoffs in the calculations presented below.

Figures 10(h)–10(k) show the calculated low-energy excitation spectra of $^{13}_{\Lambda}$C, in comparison with the corresponding data. One can see that the low-lying spectra for $^{13}_{\Lambda}$C are reproduced rather well, although the excitation energies are slightly overestimated.

In the coupled-channels calculation, the doublets $(5/2^+,3/2^+)$ and $(9/2^+,7/2^+)$ in Fig. 10(h) mainly consist of the configuration of $\Lambda s_{1/2}\otimes 2^+_1$ and $\Lambda s_{1/2}\otimes 4^+_1$, respectively. See Table II for the probabilities for the dominant components in each state. These doublets are degenerate in the single-channel calculation, as already shown in Fig. 10(d). The states of $3/2^+$ and $5/2^+$ are different from each other by 10 keV due to the weak mixing of other configurations. The levels in Fig. 10(i) correspond to the configuration of $\Lambda s_{1/2}$ coupled to the second band ($n=2$) in ^{12}C. These levels share similar features as those in Fig. 10(h).

The negative-parity states are shown in Figs. 10(j) and 10(k). The energy splitting between the $3/2^-$ and $1/2^-$ states is as small as 199 keV. Notice that in the single-channel calculation the energy difference between the pure configurations of $\Lambda_{p3/2}\otimes 0^+_1$ and $\Lambda_{p1/2}\otimes 0^+_1$ is 180 keV. That is, the energy splitting of $3/2^-$ and $1/2^-$ states reflects mainly the spin-orbit splitting of Λ hyperon in the $p_{3/2}$ and $p_{1/2}$ states. A small splitting between the $3/2^-$ and $1/2^-$ states has been shown also in our previous calculation for $^{9}_{\Lambda}$Be [27], although it does not reflect the Lambda spin-orbit splitting because of a strong mixing between the $\Lambda_{p_{1/2}}\otimes 0^+$ and the $\Lambda_{p_{3/2}}\otimes 2^+$ configurations in the $1/2^-$ state.

For the second $1/2^-$ and $3/2^-$ states, one can see a large configuration mixing (see Table II). This is because there are two states whose unperturbed energy in the single-channel calculations, $E^{(0)}_{\rm 1ch}$, is close to one another. These two states are strongly coupled due to the off-diagonal components of the coupling potentials in the coupled-channels equations. Notice that, in $^{9}_{\Lambda}$Be, this happens already in the first $1/2^-$ state [27], because the reorientation effect discussed in the previous subsection brings the $\Lambda_{p_{3/2}}\otimes 2^+$ configuration close to the $\Lambda_{p_{1/2}}\otimes 0^+$ configuration in energy due to the prolate nature of the 2^+ state of ^{8}Be.

According to our calculation, the experimentally observed level at excitation energy of 11.8 MeV has the spin parity of $1/2^+$, dominated by the configuration $\Lambda_{s1/2}\otimes 0^+_2$ [cf. Fig. 10(e)] or the first radial excitation state of the configuration $\Lambda_{s1/2}\otimes 0^+_1$ [cf. Fig. 10(d)].

Figure 13 shows a comparison of low-energy excitation spectra of $^{13}_{\Lambda}$C obtained with the present microscopic particle-rotor model (MPRM), the multichannel algebraic scattering (MCAS) approach [55], and the $3\alpha+\Lambda$ cluster model [56], together with the experimental data [1]. The basic idea of MCAS approach for Λ hypernuclei [55] is similar to the microscopic PRM model in a sense that the hypernuclear wave function is given by the Λ hyperon coupled to the low-lying states of nuclear core. In contrast to our full microscopic models, in which all the inputs are from the multireference CDFT calculation, the MCAS approach adopts the experimental data for the energies of nuclear core states

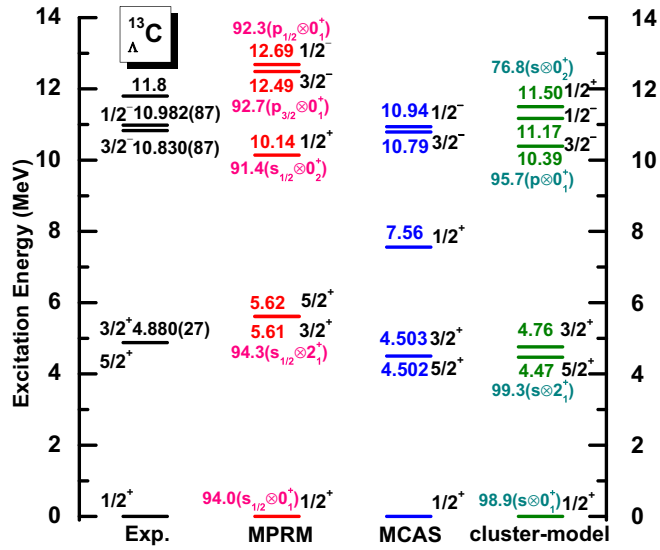

FIG. 13. (Color online) A comparison of low-energy excitation spectra of $^{13}_{\Lambda}$C obtained with the present microscopic particle-rotor model (MPRM), the multi-channel algebraic scattering (MCAS) approach [55], the $3\alpha+\Lambda$ cluster model [56], and the experimental data [1].

TABLE III. The calculated $E2$ transition strengths (in units of e^2 fm^4) for low-lying positive-parity states of ^{12}C and $^{13}_{\Lambda}$C. The c$B(E2)$ values are calculated according to Eq. (33). The changes in the $B(E2)$ are indicated with the quantity defined by $\Delta \equiv (cB(E2) - B(E2;{}^{12}\mathrm{C}))/B(E2;{}^{12}\mathrm{C})$. The value in the parenthesis for ^{12}C is the experimental data taken from Ref. [50].

^{12}C		$^{13}_{\Lambda}$C			
$I_i^\pi \to I_f^\pi$	$B(E2)$	$J_i^\pi \to J_f^\pi$	$B(E2)$	$cB(E2)$	$\Delta(\%)$
$2_1^+ \to 0_1^+$	6.62	$3/2_1^+ \to 1/2_1^+$	5.68	5.68	−14.17
	(7.6 ± 0.4)	$5/2_1^+ \to 1/2_1^+$	5.68	5.68	−14.17
$4_1^+ \to 2_1^+$	14.60	$7/2_1^+ \to 3/2_1^+$	10.34	11.48	−21.36
		$7/2_1^+ \to 5/2_1^+$	1.15	11.49	−21.35
		$9/2_1^+ \to 5/2_1^+$	11.48	11.48	−21.36

with an assumption of a pure collective rotational states and a phenomenological deformed Woods-Saxon potential for the coupling potentials. In contrast to the MCAS approach and cluster model calculation, the ordering of the first degenerate $3/2^+$ and $5/2^+$ states are not reproduced in the microscopic PRM calculation, since we do not include a spin-spin interaction in our calculation. Except for this, the ordering of low-lying states and the structure of spectrum are the same between the microscopic PRM and the MCAS approach. The main components of each state obtained with the microscopic PRM calculation are similar to those in the cluster model calculation.

Table III shows the calculated $E2$ transition strengths for low-lying positive-parity states of the hypernucleus and the corresponding core nucleus. In order to remove the trivial factor due to the angular momentum coupling for $s_{1/2}$ for the Λ particle and see more clearly the impurity effect of Λ particle on nuclear collectivity, we define the c$B(E2)$ value (that is, the $B(E2)$ value for the core part) as

$$cB(E2: I_i \to I_f) \equiv \hat{I}_i^{-2} \hat{J}_f^{-2} \begin{Bmatrix} I_f & J_f & j_i \\ J_i & I_i & 2 \end{Bmatrix}^{-2} \times B(E2: J_i \to J_f), \quad (33)$$

where j_i is the value for the main channel in the initial state. The impurity effect of Λ particle can be discussed by comparing the $B(E2)$ values for the core nucleus and the c$B(E2)$ values for the corresponding hypernucleus. One can see that the $E2$ transition strength for $2_1^+ \to 0_1^+$ in ^{12}C is significantly reduced, by a factor of ∼14%, due to the addition of a Λ particle.

B. Low-energy spectroscopy of $^{21}_{\Lambda}$Ne

We next consider an application to hypernuclei in the sd-shell region. For this purpose, we discuss the $^{21}_{\Lambda}$Ne hypernucleus. Since the Λ binding energy in $^{21}_{\Lambda}$Ne has not yet been measured, we fit the value of coupling strength parameters $\alpha_S^{N\Lambda}$ and $\alpha_V^{N\Lambda}$ to the Λ binding energy estimated with a deformed relativistic mean field calculation [23]. With the PC-F1 and PCY-S1 forces for NN and $N\Lambda$ interactions, respectively, B_Λ is estimated to be 14.35 MeV for the lowest Λ hyperon state. With the same process as in Sec. III A 2, we obtain a parameter set of $\alpha_S^{N\Lambda} = -4.2377 \times 10^{-5}$ MeV^{-2} and $\alpha_V^{N\Lambda} = 1.6694 \times 10^{-5}$ MeV^{-2}.

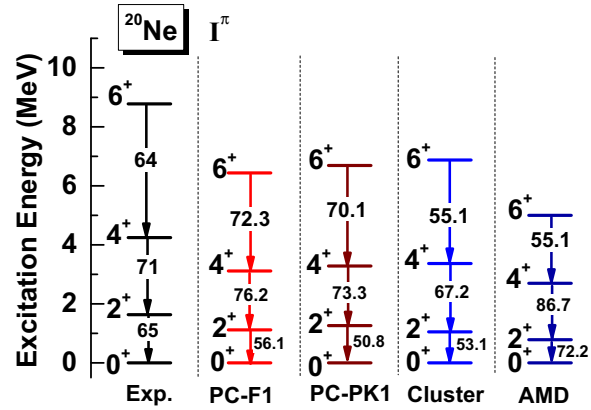

FIG. 14. (Color online) A comparison of the yrast rotational states of ^{20}Ne obtained with several methods. The results of the cluster model and the AMD are taken from Refs. [57] and [14], respectively.

Figure 14 shows the calculated yrast rotational states of ^{20}Ne. In order to see the parameter set dependence for the NN interaction, we use both PC-F1 and PC-PK1 parameter sets. For a comparison, the figure also shows the results of $\alpha + ^{16}$O cluster model [57] and the AMD model [14]. One sees that all these models reproduce the rotational character of the yrast states, although they tend to overestimate the moment of inertia.

Figure 15 shows the obtained energy curve $E_J(\beta)$ for the $J^\pi = 1/2^+$ and $1/2^-$ states in $^{21}_{\Lambda}$Ne as a function of the deformation β of the core nucleus. The left and the right panels show the result with PC-F1 and PC-PK1 forces, respectively. For the latter, we use the same $N\Lambda$ interaction as in the former calculation, even though the parameters are determined with PC-F1. We have confirmed that this yields the B_Λ value of 14.33 MeV with PC-PK1, which is similar to the value with the PC-F1 set, that is, 14.35 MeV. For PC-F1, the hypernuclear energy curve with spin-parity of $1/2^+$ and $1/2^-$ has a prolate minimum with a smaller β than that of ^{20}Ne with 0^+. For PC-PK1, on the other hand, the value of β at the energy minimum remains almost the same for the $1/2^+$ configuration while that for the $1/2^-$ configuration increases as compared to the deformation for ^{20}Ne with 0^+. Notice that the energy surface for $1/2^-$ has a higher barrier at the spherical shape than the barrier for ^{20}Ne for both the interactions. This indicates that $^{21}_{\Lambda}$Ne with $1/2^+$ and $1/2^-$ has a smaller and a larger collectivity than that of ^{20}Ne, as in $^{13}_{\Lambda}$C. The energy differences between the $1/2^+$ state in $^{21}_{\Lambda}$Ne and the ground state of ^{20}Ne, as well as the $1/2^-$ state in $^{21}_{\Lambda}$Ne and the ground state of ^{20}Ne, are shown in Figs. 15(c) and 15(d). Even though PC-F1 and PC-PK1 forces predict somewhat different energy curves, those energy curves are qualitatively similar to each other, especially when those are plotted with respect to the energy curve for ^{20}Ne.

Figure 16 shows the spectra of both ^{20}Ne and $^{21}_{\Lambda}$Ne. To examine the channel-coupling effect on hypernuclear states, we also include the results from single-channel calculations. The figure only shows the results with PC-F1, since the results with PC-PK1 are similar (see also Fig. 18 below). The probability of the main components is summarized in Table IV.

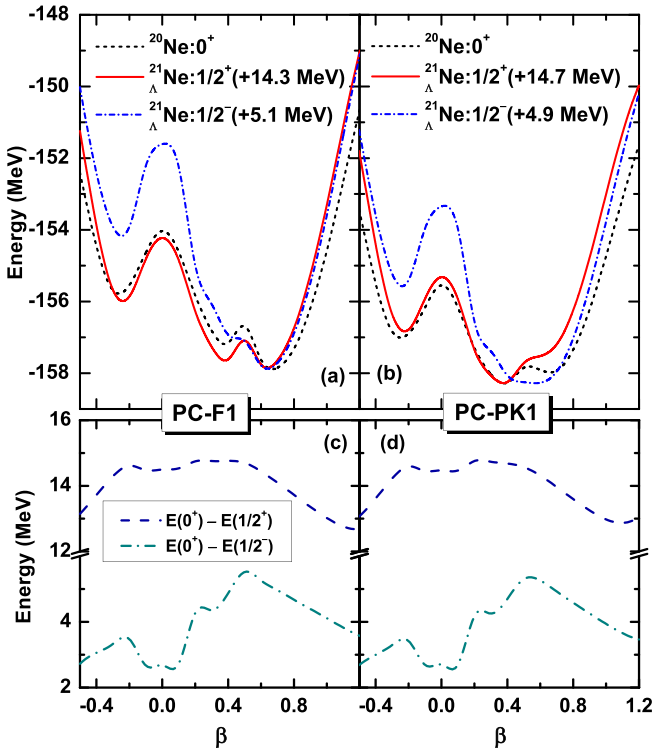

FIG. 15. (Color online) Energy curve $E_J(\beta)$ for the $J^\pi = 1/2^+$ (solid line) and $1/2^-$ (dot-dashed line) states in $^{21}_{\Lambda}$Ne as a function of the deformation β of the core nucleus. These are obtained with PC-F1 (left panel) and PC-PK1 (right panel) forces. In order to make a comparison easy, each hypernuclear curve is shifted by a constant value so that the energy at the absolute minimum coincides with that for ^{20}Ne with $I^\pi = 0^+$. The difference between the energy curve of $^{21}_{\Lambda}$Ne and that of ^{20}Ne is shown in the panels (c) and (d) for the PC-F1 and PC-PK1 forces, respectively.

It is shown that the hypernuclear states with positive parity plotted in the columns (i) and (j) from the full coupled-channels calculation are close to the results of single-channel calculation shown in the columns (e) and (f). The analysis of hypernuclear wave functions demonstrates that these states are dominated by the configuration of $\Lambda_{s1/2}$ coupled to the state I in the first ($n = 1$) and the second ($n = 2$) bands in ^{20}Ne, respectively, with the weight between 98% and 99%. It is seen that the hypernuclear

TABLE IV. Same as Table II, but for $^{21}_{\Lambda}$Ne hypernucleus with the PC-F1 and PC-PK1 forces.

		PC-F1			PC-PK1		
J^π	$(lj)\otimes I_n^\pi$	E	P_{jlI_n}	$E^{(0)}_{\rm 1ch}$	E	P_{jlI_n}	$E^{(0)}_{\rm 1ch}$
$1/2^+_1$	$s_{1/2}\otimes 0^+_1$	0.00	0.98	0	0.0	0.98	0.0
$3/2^+_1$	$s_{1/2}\otimes 2^+_1$	1.18	0.98	1.15	1.35	0.98	1.30
$5/2^+_1$	$s_{1/2}\otimes 2^+_1$	1.18	0.98	1.15	1.35	0.98	1.30
$7/2^+_1$	$s_{1/2}\otimes 4^+_1$	3.08	0.99	3.06	3.24	0.98	3.20
$9/2^+_1$	$s_{1/2}\otimes 4^+_1$	3.09	0.99	3.06	3.24	0.98	3.20
$1/2^+_2$	$s_{1/2}\otimes 0^+_2$	5.61	0.99	5.47	5.24	0.99	5.02
$3/2^+_2$	$s_{1/2}\otimes 2^+_2$	8.36	0.99	8.19	8.27	0.99	8.04
$5/2^+_2$	$s_{1/2}\otimes 2^+_2$	8.36	0.99	8.19	8.27	0.99	8.04
$1/2^-_1$	$p_{3/2}\otimes 2^+_1$	9.52	0.54	11.67	9.55	0.52	11.75
	$p_{1/2}\otimes 0^+_1$		0.42	12.03		0.45	11.87
$3/2^-_1$	$p_{3/2}\otimes 0^+_1$	9.48	0.46	11.80	9.50	0.48	11.64
	$p_{3/2}\otimes 2^+_1$		0.26	12.94		0.25	13.00
	$p_{1/2}\otimes 2^+_1$		0.24	13.17		0.23	13.23
$5/2^-_1$	$p_{1/2}\otimes 2^+_1$	10.91	0.46	13.17	10.98	0.45	13.23
	$p_{3/2}\otimes 4^+_1$		0.36	13.93		0.37	14.00
	$p_{3/2}\otimes 2^+_1$		0.15	13.81		0.15	13.87
$7/2^-_1$	$p_{3/2}\otimes 2^+_1$	10.85	0.63	12.58	10.92	0.63	12.65
	$p_{1/2}\otimes 4^+_1$		0.19	15.07		0.19	15.15
	$p_{3/2}\otimes 4^+_1$		0.15	15.19		0.15	15.28

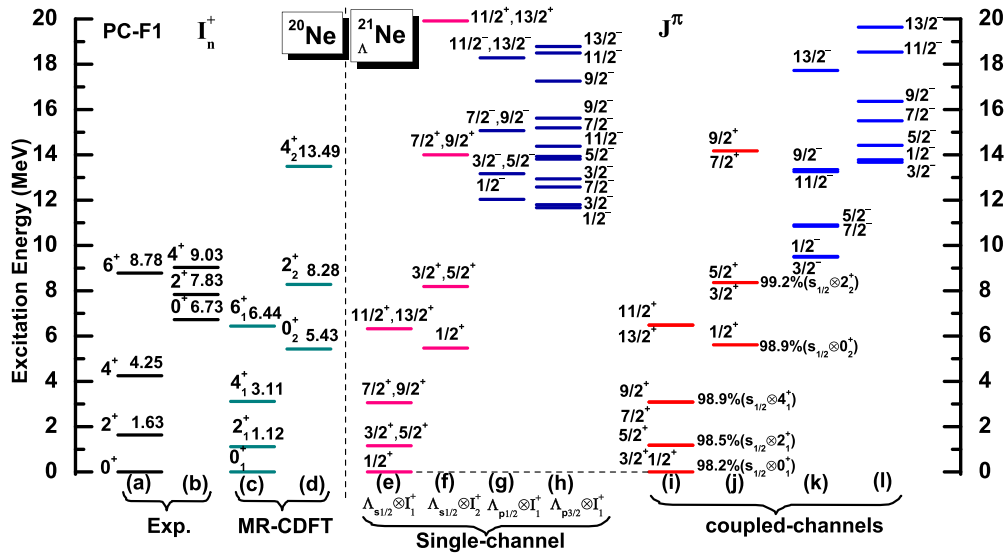

FIG. 16. (Color online) The low-energy excitation spectra of ^{20}Ne and $^{21}_{\Lambda}$Ne obtained with the microscopic particle-rotor model calculations.

doublet states $(\frac{2I-1}{2}, \frac{2I+1}{2})^{\pi}$ with configuration $\Lambda_{\ell 1/2} \otimes I^{+}$ are degenerate, as discussed in Sec. III A 4. Moreover, it is seen that the spectra of positive-parity states in ${}^{21}_{\Lambda}$Ne are close to that of ^{20}Ne with similar excitation energies to each other. In other words, the presence of a $\Lambda_{s1/2}$ does not change significantly the low-energy structure of the core nucleus ^{20}Ne.

The negative-parity states in ${}^{21}_{\Lambda}$Ne are shown in the columns (k) and (l). One can see that the channel-coupling effect plays an important role in their excitation energies. Moreover, we note that the energy difference between the first $1/2^{-}$ and $3/2^{-}$ states is less than 40 keV. Notice that the $1/2^{-}$ state is a strong admixture of the configurations $\Lambda_{p1/2} \otimes 0^{+}_{1}$ and $\Lambda_{p3/2} \otimes 2^{+}_{1}$. On the other hand, the $3/2^{-}$ state is a strong admixture of the configurations $\Lambda_{p3/2} \otimes 0^{+}_{1}$, $\Lambda_{p3/2} \otimes 2^{+}_{1}$, and $\Lambda_{p1/2} \otimes 2^{+}_{1}$. Therefore, the splitting of the $1/2^{-}$ and $3/2^{-}$ levels in ${}^{21}_{\Lambda}$Ne does not reflect the strength of Λ spin-orbit interaction, which is in marked difference from the case in ${}^{13}_{\Lambda}$C. From yet another point of view, it is interesting to point out that a typical rotational band having $L^{\pi} = 1^{-}, 3^{-}, 5^{-}, \ldots$ is realized as seen in Fig. 16(k), apart from the spin of the hyperon. This group can be characterized by the $K^{\pi} = 0^{-}$ band based on the strong coupling between the nuclear rotation and the hyperon in the p state, and thus this band manifests a genuinely hypernuclear state with the [5](90) symmetry which is similar to the [5](50) band verified in ${}^{9}_{\Lambda}$Be [3]. This feature of negative parity states in hypernuclei has already been discussed in Ref. [58] with the traditional particle-rotor model with the Elliot SU(3) model for the core states. A similar feature is found also in ${}^{155}_{\Lambda}$Sm.

The underlying reason for the difference between ${}^{13}_{\Lambda}$C and ${}^{21}_{\Lambda}$Ne is due to the different properties of the core nuclei. ^{20}Ne is well deformed with a much larger transition density $\rho^{02}_{2}(r)$ than that in ^{12}C. Notice also that the ordering of the $\Lambda_{p3/2} \otimes 2^{+}_{1}$ multiplet states is opposite to that in ${}^{13}_{\Lambda}$C, reflecting the fact that the sign of quadrupole moment is opposite (that is, prolate deformation for ^{20}Ne and oblate deformation for ^{12}C). In Fig. 17, we plot the transition density for the ${}^{21}_{\Lambda}$Ne hypernucleus. One can see that the $\lambda = 2$ component has the opposite sign as compared to the transition density for ${}^{13}_{\Lambda}$C shown in Fig. 11. Similar to the ${}^{9}_{\Lambda}$Be case, these result in several $1/2^{-}$ and $3/2^{-}$ states close in energy in

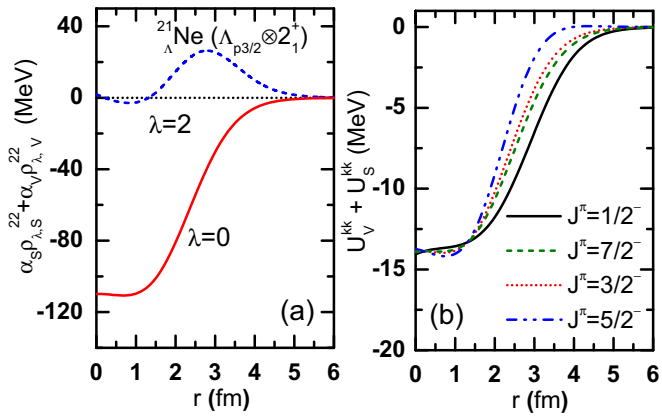

FIG. 17. (Color online) Same as Fig. 11, but for ${}^{21}_{\Lambda}$Ne.

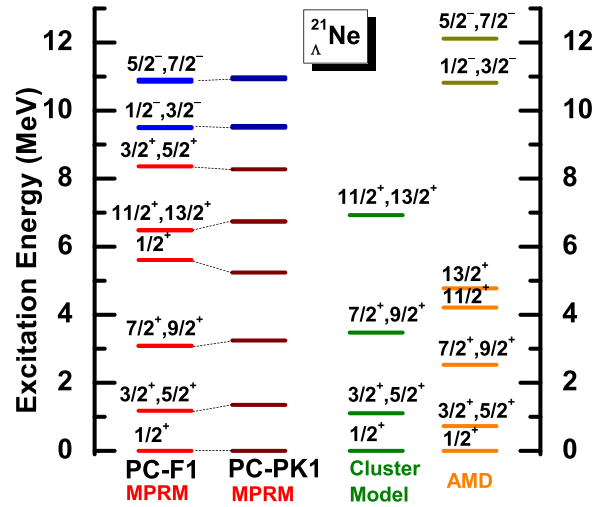

FIG. 18. (Color online) A comparison of low-energy excitation spectra of ${}^{21}_{\Lambda}$Ne obtained with the cluster model [57], the AMD [14], and the present microscopic particle-rotor model (MPRM) calculations with the PC-F1 and PC-PK1 forces.

the single-channel calculations, which are strongly mixed in the full coupled-channels treatment. Similarly to the $1/2^{-}$ and $3/2^{-}$ states, the $5/2^{-}$ and $7/2^{-}$ states also show the strong configuration mixing between Λ hyperon in $p_{1/2}$ and $p_{3/2}$ orbits. We have found that this feature of strong mixing found in ${}^{9}_{\Lambda}$Be and ${}^{21}_{\Lambda}$Ne persists also in heavier systems, such as ${}^{31}_{\Lambda}$Si and ${}^{155}_{\Lambda}$Sm.

Notice that the ^{20}Ne nucleus has prominent negative-parity bands originated from the $\alpha + {}^{16}$O structure. For simplicity, in the present calculations, we have assumed reflection symmetry for ^{20}Ne. The inclusion of these negative-parity states in the coupled-channels calculations is thus beyond the scope of the present paper. It would be an interesting future work to include them and study how the negative-parity states in ${}^{21}_{\Lambda}$Ne are perturbed.

Figure 18 shows a comparison of low-energy excitation spectra of ${}^{21}_{\Lambda}$Ne obtained with the cluster model [57], the AMD [14], and the present microscopic PRM calculations based on the PC-F1 and PC-PK1 interactions. The positive-parity band in the microscopic PRM is closer to the result of cluster model as compared to the result of AMD, which has a slightly larger moment of inertia. The negative-parity states are similar to the AMD results but with lower excitation energies, which might be due to the large channel-coupling effect taken explicitly into account in the present work; see Fig. 16 and Table IV.

Table V lists the $E2$ transition strengths for low-lying states of ${}^{21}_{\Lambda}$Ne with PC-F1. For comparison, the table also shows the change in $B(E2)$ from ^{20}Ne to ${}^{21}_{\Lambda}$Ne obtained with the PC-PK1 force, the cluster model [57], and the AMD [14]. The $B(E2)$ value decreases by adding a Λ hyperon in s orbit in these calculations. However, the cluster model and AMD model predict more reduction compared to the microscopic PRM. A further study would be necessary in order to reconcile this difference.

TABLE V. The calculated $E2$ transition strengths (in units of e^2 fm^4) for low-lying states of $^{21}_{\Lambda}$Ne with the PC-F1 force for the core states. The results for the change in the $B(E2)$ value from ^{20}Ne to $^{21}_{\Lambda}$Ne is compared with the results with PC-PK1, the cluster model [57], and the AMD [14] calculations, where Δ is defined in the caption of Table III.

Transition	PC-F1			PC-PK1	AMD	Cluster
$J_i^\pi \to J_f^\pi$	$B(E2)$	$cB(E2)$	Δ(%)	Δ(%)	Δ(%)	Δ(%)
$3/2_1^+ \to 1/2_1^+$	54.28	54.28	−3.19	−7.16	−11.8	−23.9
$5/2_1^+ \to 1/2_1^+$	54.28	54.28	−3.19	−7.16	−11.5	
$7/2_1^+ \to 3/2_1^+$	65.90	73.22	−3.95	−4.80	−17.8	−22.6
$7/2_1^+ \to 5/2_1^+$	7.32	73.22	−3.95	−4.80		
$9/2_1^+ \to 5/2_1^+$	73.22	73.22	−3.95	−4.81	−13.0	

We have also applied the microscopic particle-rotor model to study another sd-shell hypernucleus, $^{31}_{\Lambda}$Si. We have found that the impurity effect of Λ hyperon in $^{31}_{\Lambda}$Si is qualitatively the same as that in $^{21}_{\Lambda}$Ne.

C. Low-energy spectroscopy of $^{155}_{\Lambda}$Sm

One of the advantages of the microscopic particle-rotor model is that this method is not limited to light hypernuclei but it can also be applied to medium-heavy and heavy hypernuclei. As an example of application to heavy deformed hypernuclei, we next consider ^{154}Sm and $^{155}_{\Lambda}$Sm. By fitting to $B_\Lambda = 24.98$ MeV estimated with the deformed RMF calculation, we obtain a parameter set of ΛN interaction as $\alpha_S^{N\Lambda} = -4.2377 \times 10^{-5}$ MeV^{-2} and $\alpha_V^{N\Lambda} = 1.0401 \times 10^{-5}$ MeV^{-2}. Figure 19 shows the projected energy curves for ^{154}Sm and $^{155}_{\Lambda}$Sm obtained with this $N\Lambda$ interaction together with PC-F1 for the NN interaction. For the $1/2^+$ state, the polarization effect of Λ particle in s orbit on the properties of ^{154}Sm is much smaller than that on ^{12}C and ^{20}Ne due to the large mass number, although the effect is still large for the negative-parity states due to the strong channel coupling effects.

Figure 20 shows the calculated low-energy spectrum of ^{154}Sm and $^{155}_{\Lambda}$Sm with the PC-F1 force. The ground-state band and the two β bands in ^{154}Sm are reasonably reproduced,

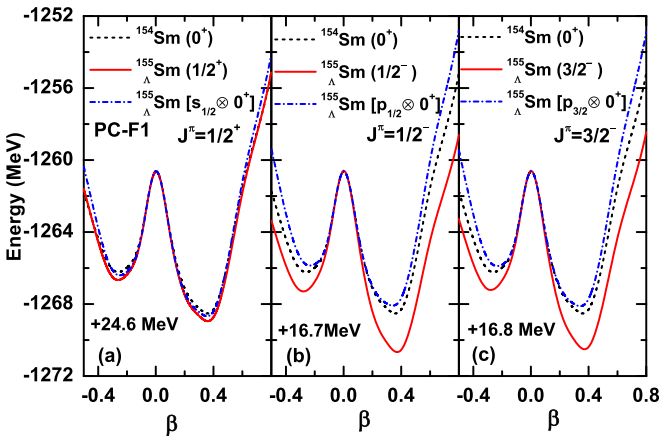

FIG. 19. (Color online) Same as Fig. 9, but for ^{154}Sm and $^{155}_{\Lambda}$Sm.

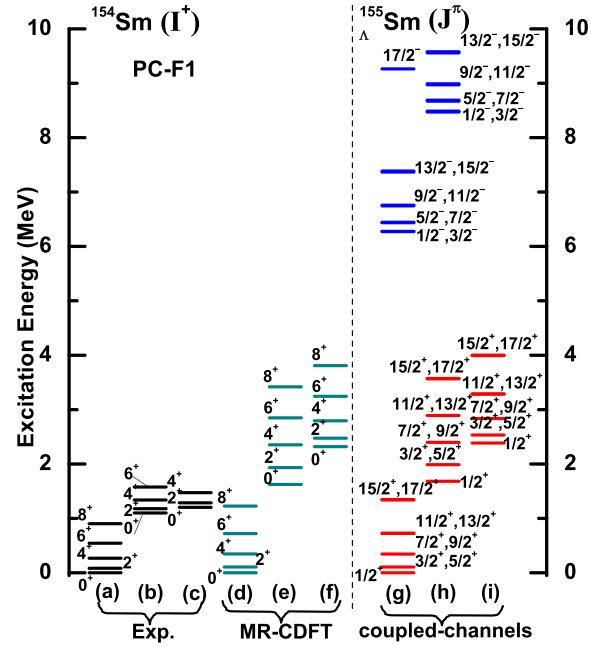

FIG. 20. (Color online) Low-energy excitation spectra of ^{154}Sm [(a)–(f)] and $^{155}_{\Lambda}$Sm [(g)–(i)].

although the bandhead energy of the β bands are overestimated. The low-lying positive-parity states J^π in $^{155}_{\Lambda}$Sm are dominated by the single configuration of $\Lambda_{s_{1/2}} \otimes I^+$ with similar excitation energy as that of the nuclear core state with I^+. As shown in Table VI, the positive-parity states J^+, except

TABLE VI. Same as Table II, but for $^{155}_{\Lambda}$Sm hypernuclei.

J^π	E	$(lj) \otimes I_n^\pi$	P_{jlI_n}	$E_{\rm 1ch}^{(0)}$
$1/2_1^+$	0.00	$s_{1/2} \otimes 0_1^+$	0.98	0.00
$3/2_1^+$	0.11	$s_{1/2} \otimes 2_1^+$	0.98	0.11
$5/2_1^+$	0.11	$s_{1/2} \otimes 2_1^+$	0.98	0.11
$7/2_1^+$	0.35	$s_{1/2} \otimes 4_1^+$	0.98	0.35
$9/2_1^+$	0.35	$s_{1/2} \otimes 4_1^+$	0.98	0.35
$1/2_2^+$	1.68	$s_{1/2} \otimes 0_2^+$	0.99	1.58
$3/2_2^+$	1.99	$s_{1/2} \otimes 2_2^+$	0.99	1.90
$5/2_2^+$	1.99	$s_{1/2} \otimes 2_2^+$	0.99	1.90
$1/2_1^-$	6.28	$p_{3/2} \otimes 2_1^+$	0.66	7.58
		$p_{1/2} \otimes 0_1^+$	0.32	8.51
$3/2_1^-$	6.27	$p_{3/2} \otimes 0_1^+$	0.35	8.31
		$p_{3/2} \otimes 2_1^+$	0.32	8.42
		$p_{1/2} \otimes 2_1^+$	0.29	8.61
$5/2_1^-$	6.44	$p_{3/2} \otimes 4_1^+$	0.53	8.08
		$p_{1/2} \otimes 2_1^+$	0.33	8.61
		$p_{3/2} \otimes 2_1^+$	0.11	8.96
$7/2_1^-$	6.44	$p_{3/2} \otimes 2_1^+$	0.47	8.19
		$p_{1/2} \otimes 4_1^+$	0.28	8.86
		$p_{3/2} \otimes 4_1^+$	0.22	8.89

TABLE VII. Same as Table III, but for ^{154}Sm and $^{155}_{\Lambda}$Sm. The experimental data for ^{154}Sm, shown in the parentheses, are taken from Ref. [59].

^{154}Sm		$^{155}_{\Lambda}$Sm			
$I_i^\pi \to I_f^\pi$	$B(E2)$	$J_i^\pi \to J_f^\pi$	$B(E2)$	$cB(E2)$	$\Delta(\%)$
$2_1^+ \to 0_1^+$	9358.49	$3/2_1^+ \to 1/2_1^+$	9284.69	9284.69	−0.79
	(8720 ± 100)	$5/2_1^+ \to 1/2_1^+$	9284.23	9284.23	−0.79
$4_1^+ \to 2_1^+$	13512.18	$7/2_1^+ \to 3/2_1^+$	12081.04	13423.38	−0.66
		$7/2_1^+ \to 5/2_1^+$	1342.25	13422.54	−0.66
		$9/2_1^+ \to 5/2_1^+$	13422.25	13422.25	−0.67

for $1/2^+$, are nearly twofold degenerate. These characters are similar to the hypernuclei in the light-mass region. On the other hand, one can see that the negative-parity bands are well separated from the positive-parity ground band in $^{155}_{\Lambda}$Sm, which is different from the light hypernuclei. It is because the energy scale of the rotational motion is proportional to $A^{-7/3}$ (see Eq. (1.50) in Ref. [38]), while that of single-Λ excitation from s to p orbit is proportional to $A^{-1/3}$. Therefore, with the increase of mass number A, the rotational energy spectrum is compressed faster than the single-Λ excitation spectrum. Besides, the low-lying negative-parity states J^- are nearly twofold degenerate, even though there are strong configuration mixing in these states.

Table VII presents the $E2$ transition strengths in ^{154}Sm and $^{155}_{\Lambda}$Sm. It is shown that the change in the $B(E2)$ values by adding a Λ hyperon in s orbital is less than 1%, which is much smaller than that in the light hypernuclei studied in this paper. This is consistent with the small polarization effect of Λ particle discussed in connection to the projected energy surface shown in Fig. 19.

IV. SUMMARY

We have presented the detailed formalism of the microscopic particle rotor model based on a covariant density functional theory for the low-lying states of single-Λ hypernuclei. In this formalism, the wave functions for hypernuclei have been constructed by coupling the Λ hyperon to the low-lying states of the core nucleus. The radial wave functions are obtained by solving the corresponding coupled-channel equations, in which the coupling potentials are provided in terms of the transition densities of the nuclear core states. For simplicity, in this paper we have adopted only the leading-order four-fermion coupling terms of scalar and vector types for the ΛN effective interaction. Applying this method to $^{13}_{\Lambda}$C, we have reproduced reasonably well the experimental energy spectrum of this hypernucleus. We have applied this method also to $^{21}_{\Lambda}$Ne and $^{155}_{\Lambda}$Sm, and have achieved a good agreement with other model studies both for the excitation energies and the compositions of wave functions. We mention that no other microscopic methods have been applied so far to low-lying states of such heavy hypernuclei as $^{155}_{\Lambda}$Sm. We have found that the NN interaction with the PC-F1 and PC-PK1 sets leads to similar hypernuclei spectra to each other. For all the hypernuclei, the low-lying excited states with positive-parity J^+, except for $1/2^+$, are nearly twofold degenerate and dominated by the single configuration of $\Lambda_{s_{1/2}} \otimes I^+$, where I^+ is the spin parity of the nuclear core states. In contrast, in general there is large configuration mixing in the negative-parity states. We have, however, found an exception for this, that is, for the first $3/2^-$ and $1/2^-$ states in $^{13}_{\Lambda}$C the effect of configuration mixing is rather small, and thus the energy splitting of these states reflects the spin-orbit splitting of Λ hyperon in the $p_{3/2}$ and $p_{1/2}$ states. Concerning the electromagnetic transitions, we have found that for all the systems the $B(E2)$ value from the first 2^+ to the ground states in the core nuclei is reduced by adding a Λ particle in the positive-parity states. The reduction factor is about 14% for $^{13}_{\Lambda}$C, 3.2% for $^{21}_{\Lambda}$Ne, and 0.79% for $^{155}_{\Lambda}$Sm, and thus the reduction factor is larger for the oblate hypernuclei. For $^{21}_{\Lambda}$Ne and $^{31}_{\Lambda}$Si, a slightly larger impurity effect was found with the PC-PK1 force as compared to the PC-F1 force.

New measurements of γ-ray spectroscopy of hypernuclei will soon start at the new generation experimental facilities such as J-PARC. It would be interesting if the low-lying spectra predicted in this paper are confirmed in near future.

ACKNOWLEDGMENTS

This work was supported in part by the Tohoku University Focused Research Project "Understanding the origins for matters in universe,"JSPS KAKENHI Grant No. 26400263, the National Natural Science Foundation of China under Grants No. 11305134 and No. 11105111, and the Fundamental Research Funds for the Central University (XDJK2013C028).

[1] O. Hashimoto and H. Tamura, Prog. Part. Nucl. Phys. **57**, 564 (2006).
[2] H. Tamura, Int. J. Mod. Phys. A **24**, 2101 (2009).
[3] T. Motoba, H. Bandō, and K. Ikeda, Prog. Theor. Phys. **70**, 189 (1983).
[4] E. Hiyama, M. Kamimura, K. Miyazaki, and T. Motoba, Phys. Rev. C **59**, 2351 (1999).
[5] H. Bando, T. Motoba and J. Žofka, Int. J. Mod. Phys. A **5**, 4021 (1990).
[6] E. Hiyama, Y. Kino, and M. Kamimura, Prog. Part. Nucl. Phys. **51**, 223 (2003).
[7] E. Cravo, A. C. Fonseca, and Y. Koike, Phys. Rev. C **66**, 014001 (2002).
[8] V. M. Suslov, I. Filikhin, and B. Vlahovic, J. Phys. G: Nucl. Part. Phys. **30**, 513 (2004).
[9] M. Shoeb and Sonika, Phys. Rev. C **79**, 054321 (2009).
[10] R. H. Dalitz and A. Gal, Ann. Phys. (N.Y.) **116**, 167 (1978).
[11] A. Gal, J. M. Soper, and R. H. Dalitz, Ann. Phys. (N.Y.) **63**, 53 (1971).
[12] D. J. Millener, Nucl. Phys. A **804**, 84 (2008); **914**, 109 (2013).
[13] R. Wirth, D. Gazda, P. Navrátil, A. Calci, J. Langhammer, and R. Roth, Phys. Rev. Lett. **113**, 192502 (2014).

[14] M. Isaka, M. Kimura, A. Doté, and A. Ohnishi, Phys. Rev. C **83**, 044323 (2011).
[15] M. Isaka, M. Kimura, A. Doté, and A. Ohnishi, Phys. Rev. C **83**, 054304 (2011).
[16] M. Isaka, H. Homma, M. Kimura, A. Doté, and A. Ohnishi, Phys. Rev. C **85**, 034303 (2012).
[17] M. Isaka, M. Kimura, A. Doté, and A. Ohnishi, Phys. Rev. C **87**, 021304(R) (2013).
[18] X. R. Zhou, H.-J. Schulze, H. Sagawa, C. X. Wu, and E.-G. Zhao, Phys. Rev. C **76**, 034312 (2007).
[19] M. T. Win and K. Hagino, Phys. Rev. C **78**, 054311 (2008).
[20] H.-J. Schulze, M. T. Win, K. Hagino, and H. S. Sagawa, Prog. Theo. Phys. **123**, 569 (2010).
[21] M. T. Win, K. Hagino, and T. Koike, Phys. Rev. C **83**, 014301 (2011).
[22] B.-N. Lu, E.-G. Zhao, and S.-G. Zhou, Phys. Rev. C **84**, 014328 (2011).
[23] W. X. Xue, J. M. Yao, K. Hagino, Z. P. Li, H. Mei, and Y. Tanimura, Phys. Rev. C **91**, 024327 (2015).
[24] A. Li, E. Hiyama, X.-R. Zhou, and H. Sagawa, Phys. Rev. C **87**, 014333 (2013).
[25] B.-N. Lu, E. Hiyama, H. Sagawa, and S.-G. Zhou, Phys. Rev. C **89**, 044307 (2014).
[26] K. Hagino and J. M. Yao, arXiv:1410.7531.
[27] H. Mei, K. Hagino, J. M. Yao, and T. Motoba, Phys. Rev. C **90**, 064302 (2014).
[28] Y. Tanimura and K. Hagino, Phys. Rev. C **85**, 014306 (2012).
[29] T. Burvenich, D. G. Madland, J. A. Maruhn, and P.-G. Reinhard, Phys. Rev. C **65**, 044308 (2002).
[30] J. M. Yao, M. Bender, and P.-H. Heenen, Phys. Rev. C **91**, 024301 (2015).
[31] J. M. Yao, H. Mei, and Z. P. Li, Phys. Lett. B **723**, 459 (2013).
[32] X. Y. Wu, J. M. Yao, and Z. P. Li, Phys. Rev. C **89**, 017304 (2014).
[33] A. Edmonds, *Angular Momentum in Quantum Mechanics* (Princeton University Press, Princeton, NJ, 1957).
[34] J. M. Yao, J. Meng, P. Ring, and D. Vretenar, Phys. Rev. C **81**, 044311 (2010).
[35] J. M. Yao, H. Mei, H. Chen, J. Meng, P. Ring, and D. Vretenar, Phys. Rev. C **83**, 014308 (2011).
[36] J. M. Yao, K. Hagino, Z. P. Li, J. Meng, and P. Ring, Phys. Rev. C **89**, 054306 (2014).
[37] J. J. Griffin, J. A. Wheeler, J. J. Griffin, and J. A. Wheeler, Phys. Rev. **108**, 311 (1957).
[38] P. Ring and P. Schuck, *The Nuclear Many Body Problem* (Springer-Verlag, New York, 1980).
[39] P. W. Zhao, Z. P. Li, J. M. Yao, and J. Meng, Phys. Rev. C **82**, 054319 (2010).
[40] M. Bender, K. Rutz, P.-G. Reinhard, and J. A. Maruhn, Eur. Phys. J. A **8**, 59 (2000).
[41] P. Arumugam, B. K. Sharma, S. K. Patra, and R. K. Gupta, Phys. Rev. C **71**, 064308 (2005).
[42] J. M. Yao, N. Itagaki, and J. Meng, Phys. Rev. C **90**, 054307 (2014).
[43] A. Nakada, Y. Torizuka, and Y. Horikawa, Phys. Rev. Lett. **27**, 745 (1971).
[44] L. S. Cardman, J. W. Lightbody, S. Penner, W. P. Trower, and S. F. Williamson, Phys. Lett. B **91**, 203 (1980).
[45] Y. Fukuoka, S. Shinohara, Y. Funaki, T. Nakatsukasa, and K. Yabana, Phys. Rev. C **88**, 014321 (2013).
[46] I. Angeli, At. Data Nucl. Data Tables **87**, 185 (2004).
[47] M. Chernykh, H. Feldmeier, T. Neff, P. von Neumann-Cosel, and A. Richter, Phys. Rev. Lett. **98**, 032501 (2007).
[48] Y. Kanada-En'yo, Prog. Theor. Phys. **117**, 655 (2007).
[49] Y. Funaki, A. Tohsaki, H. Horiuchi, P. Schuck, and G. Röpke, Phys. Rev. C **67**, 051306(R) (2003).
[50] F. Ajzenberg-Selove, Nucl. Phys. A **506**, 1 (1990).
[51] T. Kibedi and R. H. Spear, At. Data Nucl. Data Tables **89**, 77 (2005).
[52] National Nuclear Data Center (NNDC) [http://www.nndc.bnl.gov/].
[53] S. Ajimura, H. Hayakawa, T. Kishimoto, H. Kohri, K. Matsuoka, S. Minami, T. Mori, K. Morikubo, E. Saji, A. Sakaguchi *et al.*, Phys. Rev. Lett. **86**, 4255 (2001).
[54] H. Kohri, S. Ajimura, H. Hayakawa, T. Kishimoto, K. Matsuoka, S. Minami, Y. S. Miyake, T. Mori, and K. Morikubo, E. Saji *et al.*, Phys. Rev. C **65**, 034607 (2002).
[55] L. Canton, K. Amos, S. Karataglidis, and J. P. Svenne, Int. J. Mod. Phys. E **19**, 1435 (2010).
[56] E. Hiyama, M. Kamimura, T. Motoba, T. Yamada, and Y. Yamamoto, Phys. Rev. Lett. **85**, 270 (2000).
[57] T. Yamada, K. Ikeda, H. Bando, and T. Motoba, Prog. Theor. Phys. **71**, 985 (1984).
[58] H. Bando, K. Ikeda, and T. Motoba, Prog. Theo. Phys. **69**, 918 (1983).
[59] J. Tauren and R. B. Firest, Evaluated Nuclear Structure Data File (ENSDF) [http://ie.lbl.gov/TOI2003/index.asp].